The Astrophysical Journal, 667:149–169, 2007 September 20 Ⓔ
© 2007. The American Astronomical Society. All rights reserved. Printed in U.S.A.

HIGH-RESOLUTION MID-INFRARED SPECTROSCOPY OF ULTRALUMINOUS INFRARED GALAXIES

D. Farrah,[1] J. Bernard-Salas,[1] H. W. W. Spoon,[1] B. T. Soifer,[2] L. Armus,[2] B. Brandl,[3]
V. Charmandaris,[4,5] V. Desai,[2] S. Higdon,[6] D. Devost,[1] and J. Houck[1]
Received 2007 March 24; accepted 2007 May 30

ABSTRACT

We present $R \sim 600$, 10–37 μm spectra of 53 ultraluminous infrared galaxies (ULIRGs), taken using the Infrared Spectrograph on board *Spitzer*. The spectra show fine-structure emission lines of neon, oxygen, sulfur, silicon, argon, chlorine, iron, and phosphorous; molecular hydrogen lines, and C_2H_2, HCN, and OH^- absorption features. We employ diagnostics based on the fine-structure lines, the polycyclic aromatic hydrocarbon (PAH) features and the 9.7 μm silicate absorption feature, to show that the infrared emission from most ULIRGs is powered mostly by star formation, with only ~20% of ULIRGs hosting an AGN with a greater IR luminosity than the starburst. The detection of [Ne v] λ14.32 in just under half the sample, however, implies that an AGN contributes significantly to the mid-IR flux in ~42% of ULIRGs. The starbursts and AGNs in ULIRGs appear more extincted, and for the starbursts more compact than those in lower luminosity systems. The excitations and electron densities in the narrow-line regions of ULIRGs appear comparable to those of starbursts with $L \lesssim 10^{11.5}\,L_\odot$, although the NLR gas in ULIRGs may be more dense. We show that the [Ne ii] λ12.81 + [Ne iii] λ15.56 luminosity correlates with both infrared luminosity and the luminosity of the 6.2 and 11.2 μm PAH features, and derive a calibration between PAH luminosity and star formation rate. Finally, we show that ULIRGs with silicate absorption strengths $S_{\rm sil}$ of $0.8 \lesssim S_{\rm sil} \lesssim 2.4$ are likely to be powered mainly by star formation, but that ULIRGs with $S_{\rm sil} \lesssim 0.8$, and possibly those with $S_{\rm sil} \gtrsim 2.4$, contain an IR-luminous AGN.

Subject headings: galaxies: active — galaxies: evolution — galaxies: starburst — infrared: galaxies

Online material: color figures

1. INTRODUCTION

Ultraluminous infrared galaxies (ULIRGs; objects with 1–1000 μm luminosities in excess of $10^{12}\,L_\odot$) were first discovered in the 1970s (Rieke & Low 1972). Since then, they have fascinated astronomers with their unique and extraordinary properties, and infuriated them with their singularly opaque natures, almost in equal measure.

In the local universe ULIRGs are a rare, if interesting, oddity, with only 50 or so examples known at $z \lesssim 0.1$. First uncovered in significant numbers by surveys with the *Infrared Astronomical Satellite* (*IRAS*; Soifer et al. 1984; Houck et al. 1985), work focused on determining the power source behind their colossal infrared emission. This initially provoked heated debate between a "starburst" camp and an "active galactic nucleus (AGN)" camp, a debate that has not yet entirely cooled. Early studies showed that some ULIRG optical spectra resembled those of starburst galaxies (Joseph & Wright 1985), whereas others contained emission lines characteristic of Seyfert galaxies (Sanders et al. 1988). Radio observations showed direct evidence for starbursts in some ULIRGs (Condon et al. 1991; Smith et al. 1998) and AGNs in others (Lonsdale et al. 2003; Nagar et al. 2003). Over the last decade or so, however, a consensus has started to emerge; local ULIRGs are likely to be "composite" objects, with most powered mainly by a starburst, but with a significant fraction also containing an IR-luminous AGN. This is suggested from several lines of evidence, including optical/UV spectroscopy (Veilleux et al. 1995, 1999; Lípari et al. 2003; Farrah et al. 2005), mid-infared spectroscopy (Lutz et al. 1996, 1998; Genzel et al. 1998; Rigopoulou et al. 1999; Genzel & Cesarsky 2000; Tran et al. 2001), modeling of their 1–1000 μm spectral energy distributions (Klaas et al. 2001; Farrah et al. 2003), and X-ray observations (Franceschini et al. 2003; Ptak et al. 2003), although some recent studies suggest a significantly greater average AGN contribution (Imanishi et al. 2007). Local ULIRGs are also associated almost exclusively with galaxy mergers (Farrah et al. 2001; Bushouse et al. 2002; Veilleux et al. 2002), and may be involved to some degree in triggering QSOs (Sanders et al. 1988; Tacconi et al. 2002; Kawakatu et al. 2006; Zauderer et al. 2007). Excellent reviews of the properties of ULIRGs can be found in Sanders & Mirabel (1996) and more recently in Lonsdale et al. (2006).

Their rarity in the local universe compared to lower luminosity systems initially led astronomers to believe that ULIRGs did not play a fundamental role in galaxy formation processes; however, this perception changed abruptly when it was realized that ULIRGs were vastly more numerous at high redshift. First hinted at by spectroscopic follow-up of *IRAS* surveys (Hacking et al. 1987; Lonsdale et al. 1990; Saunders et al. 1990), which showed strong evolution in the ULIRG luminosity function with redshift, and from the discovery of a remarkably high cosmic infrared background by *COBE* (Puget et al. 1996), this was confirmed by surveys with *ISO* (Rowan-Robinson et al. 1997; Levine et al. 1998; Dole et al. 2001; Verma et al. 2005), which found a large population of ULIRGs up to $z \sim 1.5$, and thrown into sharp relief by submillimeter surveys (Hughes et al. 1998; Eales et al. 2000; Borys et al. 2003; Coppin et al. 2006), which showed that there were several hundred ULIRGs *per square degree* at $z \gtrsim 1$. Although obviously much harder to study, these distant ULIRGs seem superficially similar to their low-redshift counterparts in that they appear to be powered by both starburst and AGN activity (Farrah et al. 2002a; Smail et al. 2003, 2004; Alexander et al. 2005; Takata et al. 2006; Valiante et al. 2007), and are probably mergers (Farrah et al. 2002b; Chapman et al. 2003). Their properties

---

[1] Department of Astronomy, Cornell University, Ithaca, NY 14853.

[2] *Spitzer* Science Center, Pasadena, CA 91125.

[3] Sterrewacht Leiden, Leiden University, 2300 RA Leiden, Netherlands.

[4] Department of Physics, University of Crete, GR-71003 Heraklion, Greece.

[5] IESL/Foundation for Research and Technology-Hellas, GR-71110, Heraklion, Greece; and Chercheur Associé, Observatoire de Paris, F-75014, Paris, France.

[6] Physics Department, Georgia Southern University, Statesboro, GA 30460.

may make them important tools in understanding the global evolution of galaxies and large-scale structures; their rapid star formation rates and comoving number densities make them strong candidates for being the rapid growth phases of massive elliptical galaxies (Scott et al. 2002; Rocca-Volmerange et al. 2004; Swinbank et al. 2006), and they may serve as efficient "lighthouses" of the seeds of massive clusters at $z \gtrsim 1.5$ (Blain et al. 2004; Farrah et al. 2006a, 2006b).

The still controversial nature of the power source in local ULIRGs, coupled with the central position that ULIRGs seem to play in several astrophysical processes at high redshift, makes it ever more important to understand the nature of the heavily obscured starburst and AGN activity in these systems. This is ideally done in the mid-infrared, directly sampling the emission from the hot dust that shrouds the central engines of ULIRGs, and using fine-structure lines, which suffer much less from extinction effects than optical or near-IR lines. The recently launched *Spitzer Space Telescope* (Werner et al. 2004) provides an ideal platform to undertake such studies, with its suite of mid-IR instruments, including the Infrared Spectrograph (Houck et al. 2004), which offers dramatic improvements in sensitivity and resolution compared to previous generation facilities. In this paper we present high-resolution mid-infrared spectra of 53 local ULIRGs, and discuss some spectral diagnostics based on their emission-line fluxes and other spectral features. We assume a spatially flat cosmology with $H_0 = 70$ km s^{-1} Mpc^{-1}, $\Omega = 1$, and $\Omega_m = 0.3$.

2. ANALYSIS

2.1. *Observations*

The ULIRGs presented here were observed as part of a large study within the IRS GTO program to obtain mid-infrared spectra of 110 low-redshift ULIRGs (*Spitzer* program ID 105). These 110 ULIRGs were selected from the *IRAS* 1 Jy (Kim & Sanders 1998) and 2 Jy (Strauss et al. 1990) spectroscopic surveys, and from the FIRST (Faint Images of the Radio Sky at Twenty cm) ULIRG sample (Stanford et al. 2000). Low-resolution spectra were obtained of all 110 objects, and high-resolution spectra were obtained of the 53 brightest (at 60 μm, those with $f_{60} > 0.7$ Jy) objects. The low-resolution spectra span 5.2–38.5 μm, with a resolution of $R \sim 60$–125. Initial results are presented in Armus et al. (2004, 2007) and Spoon et al. (2004). Molecular hydrogen masses are presented in Higdon et al. (2006), and crystalline silicate measurements are presented in Spoon et al. (2006). An atlas of the low-resolution spectra can be found in V. Desai et al. (2007, in preparation), including polycyclic aromatic hydrocarbon (PAH) luminosities and equivalent widths. Measurements of the strengths of the 9.7 μm silicate absorption features from the low-resolution spectra can be found in H. W. W. Spoon et al. (2007, in preparation).

Here we present the 53 high-resolution spectra. The sample is listed in Table 1. A few of the sample have IR luminosities that lie slightly below the canonical ULIRG lower limit of $10^{12}\,L_\odot$, but for simplicity we refer to them as ULIRGs for the remainder of this paper. Each ULIRG was observed with both the Short-High (SH; 9.9–19.6 μm, $11.3'' \times 4.7''$, $R \sim 600$, $2.3''$ pixel^{-1}) and Long-High (LH; 18.7–37.2 μm, $22.3'' \times 11.1''$, $R \sim 600$, $4.5''$ pixel^{-1}) modules onboard the infrared IRS. The targets were placed in the center of each slit by performing "high" accuracy peak-ups using the blue peak-up array, on either a nearby 2MASS star or on the nuclei of the ULIRGs themselves, and observed in two nod positions. For five ULIRGs, their nuclei are separated by distances of $\sim 5''$ or more; for IRAS 08572+3915 the slits were centered on the northwestern nucleus, for IRAS 14348$-$1447 the slits were centered on the southwestern nucleus, for IRAS 19254$-$7245 the slits were centered on the southern nucleus, for IRAS 23498+2423 the slits were centered on the northwestern nucleus, and for Mrk 463 the slits were centered on the eastern nucleus. The other ULIRGs are all either single-nucleus (in ground-based imaging) systems, or have close separation ($\lesssim 5''$) double nuclei. While the available optical spectroscopy for our sample is not homogenous, there are no examples of objects in our sample where two nuclei with clearly different optical spectral classifications fall within the IRS slits.

For most of the SH observations we observed each object for six ramps, with a ramp time of 30 s, to give a total on-source exposure time of 180 s. For the fainter targets we observed for two ramps using a ramp time of 120 s, for a total on-source exposure time of 240 s. The LH observations were the same for each object; namely, four ramps and a ramp time of 60 s, for a total on-source exposure time of 240 s.[7]

2.2. *Data Reduction*

The data were processed through the *Spitzer* Science Center's pipeline reduction software (ver. 13.2), which performs standard reduction tasks such as ramp fitting and dark current subtraction. To ensure an accurate flat-fielding correction we started our reduction from the *un*-flat-fielded (`droopres`) images. Starting with these frames, we flagged rogue and otherwise "bad" pixels using the `irsclean`[8] tool, which uses a mask of rogue pixels for each campaign to first flag and then replace rogue pixels. The individual frames were then combined into a single image, and spectra were extracted from each nod using the SMART software package (Higdon et al. 2004), using full-slit extraction. Wavelength and flux calibration were performed by dividing the extracted spectra by that of a standard star, ξ Dra, and multiplying by its template (Cohen et al. 2003). Features present in only one nod position were treated as artifacts and removed manually. The two nods were then combined. The pixels on the edge of each order (typically the first and last 12 pixels) corresponding to regions of decreased sensitivity on the array were then removed to give the final spectrum for each object. The resulting spectra were generally of excellent quality. In a few cases some slight mismatch in continuum fluxes between orders was apparent, but not to an extent that could impact the analysis of emission line fluxes.

Both the SH and LH slits are too small to allow for on-slit background subtraction. Ideally the sky continuum background (which is comprised mainly of temporally and spatially varying zodiacal light) should be subtracted using contemporaneous "sky" observations, taken with similar exposure times and as close on the sky as possible to the observations of the target. Such observations were, however, not taken for our sample. In the absence of sky observations, modeled sky fluxes can be used (Reach et al. 2003), but they are uncertain by at least a factor of 2. In this paper we are interested only in the emission line fluxes, for which background continuum subtraction is not necessary. Hence, we do not correct our spectra for contamination from sky continuum background.

We measured line fluxes and wavelengths by assuming the emitting region was a point source at the spatial resolution of the SH and LH slits, subtracting the continuum via a cubic spline fit

---

[7] Details for each observation can be found by referencing the AOR keys given in Table 1 within the Leopard software, available from the *Spitzer* Science Center.

[8] This tool is available from the SSC World Wide Web site: http://ssc.spitzer.caltech.edu.

TABLE 1

Observations Summary

ID	Galaxy	R.A. (J2000.0)	Decl. (J2000.0)	Redshift	$L_{\rm IR}$[a]	$L_{\rm radio}$[b]	AOR Key[c]
1	IRAS 00188−0856	00 21 26.5	−08 39 26.3	0.128	12.42	23.82	4962560
2	IRAS 00397−1312	00 42 15.5	−12 56 02.8	0.262	13.02	23.67	4963584
3	IRAS 01003−2238	01 02 50.0	−22 21 57.5	0.118	12.33	23.63	4964608
4	IRAS 03158+4227	03 19 12.4	+42 38 28.0	0.134	12.48	23.74	12256256
5	IRAS 03521+0028	03 54 42.1	+00 37 03.4	0.152	12.55	23.56	4968448
6	IRAS 05189−2524	05 21 01.5	−25 21 45.4	0.043	12.11	23.06	4969216
7	IRAS 06035−7102	06 02 54.0	−71 03 10.2	0.079	12.19	. . .	4969728
8	IRAS 06206−6315	06 21 01.2	−63 17 23.5	0.092	12.17	. . .	4969984
9	IRAS 07598+6508	08 04 33.1	+64 59 48.6	0.148	12.56	24.31	4971008
10	IRAS 08311−2459	08 33 20.6	−25 09 33.7	0.100	12.40	24.21	4971520
11	IRAS 08572+3915	09 00 25.4	+39 03 54.4	0.058	12.12	22.51	4972032
12	IRAS 09022−3615	09 04 12.7	−36 27 01.1	0.060	12.26	23.84	4972288
13	IRAS 10378+1109	10 40 29.2	+10 53 18.3	0.136	12.35	23.56	4974336
14	IRAS 10565+2448	10 59 18.1	+24 32 34.3	0.043	12.01	23.37	4974848
15	IRAS 11095−0238	11 12 03.4	+02 04 22.4	0.107	12.29	23.81	4975360
16	IRAS 11119+3257	11 14 38.9	+32 41 33.3	0.189	12.69	24.96	4975616
17	IRAS 12018+1941	12 04 24.5	+19 25 10.3	0.169	12.54	23.61	4976640
18	IRAS 12071−0444	12 09 45.1	−05 01 13.9	0.128	12.44	23.48	4977408
19	IRAS 12514+1027	12 54 00.8	+10 11 12.4	0.319[d]	12.72	24.33	4978432
20	IRAS 13120−5453	13 15 06.4	−55 09 22.7	0.031	12.26	. . .	4978944
21	IRAS 13218+0552	13 24 19.9	+05 37 04.7	0.205	12.73	23.69	4979200
22	IRAS 13342+3932	13 36 24.1	+39 17 31.1	0.179	12.47	23.65	4979456
23	IRAS 13451+1232	13 47 33.3	+12 17 24.2	0.121	12.37	26.26	4980480
24	IRAS 14070+0525	14 09 31.3	+05 11 31.8	0.264	12.88	23.91	4980992
25	IRAS 14348−1447	14 37 38.4	−15 00 22.8	0.083	12.26	23.75	4981248
26	IRAS 14378−3651	14 40 59.0	−37 04 32.0	0.068	12.07	23.50	4981504
27	IRAS 15001+1433	15 02 31.9	+14 21 35.1	0.163	12.48	23.99	4982272
28	IRAS 15206+3342	15 22 38.0	+33 31 35.9	0.124	12.27	23.58	4982784
29	IRAS 15250+3609	15 26 59.4	+35 58 37.5	0.055	12.04	22.95	4983040
30	IRAS 15462−0450	15 48 56.8	−04 59 33.6	0.100	12.24	23.47	4984064
31	IRAS 16090−0139	16 11 40.5	−01 47 05.6	0.134	12.58	23.96	4984576
32	IRAS 17179+5444	17 18 54.2	+54 41 47.3	0.147	12.30	25.21	4986368
33	IRAS 17208−0014	17 23 22.0	−00 17 00.9	0.043	11.94	23.63	4986624
34	IRAS 19254−7245	19 31 21.6	−72 39 22.0	0.063	12.19	24.26	12256512
35	IRAS 19297−0406	19 32 21.3	−03 59 56.3	0.086	12.37	23.64	4988672
36	IRAS 20087−0308	20 11 23.9	−02 59 50.7	0.106	12.34	24.53	4989440
37	IRAS 20100−4156	20 13 29.5	−41 47 34.9	0.130	12.52	23.90	4989696
38	IRAS 20414−1651	20 44 18.2	−16 40 16.2	0.087	12.18	23.61	4989952
39	IRAS 20551−4250	20 58 26.8	−42 39 00.3	0.043	12.00	23.11	4990208
40	IRAS 22491−1808	22 51 49.3	−17 52 23.5	0.078	12.11	22.91	4990976
41	IRAS 23128−5919	23 15 46.8	−59 03 15.6	0.045	11.97	. . .	4991744
42	IRAS 23230−6926	23 26 03.6	−69 10 18.8	0.106	12.25	. . .	4992000
43	IRAS 23253−5415	23 28 06.1	−53 58 31.0	0.130	12.37	. . .	4992256
44	IRAS 23365+3604	23 39 01.3	+36 21 08.7	0.064	12.14	23.36	4992512
45	IRAS 23498+2423	23 52 26.0	+24 40 16.7	0.212	12.51	23.85	4992768
46	Mrk 1014	01 59 50.2	+00 23 40.6	0.163	12.63	24.22	4966144
47	UGC 5101	09 35 51.7	+61 21 11.3	0.039	11.96	23.73	4973056
48	3C 273	12 29 06.7	+02 03 08.6	0.158	12.83	27.47	4978176
49	Mrk 231	12 56 14.2	+56 52 25.2	0.042	12.51	24.08	4978688
50	Mrk 273	13 44 42.1	+55 53 12.7	0.038	12.09	23.63	4980224
51	Mrk 463	13 56 02.9	+18 22 19.1	0.050	11.80	24.33	4980736
52	Arp 220	15 34 57.1	+23 30 11.5	0.018	12.08	23.34	4983808
53	NGC 6240	16 52 58.9	+02 24 03.4	0.024	11.85	23.92	4985600

Note.—Units of right ascension are hours, minutes, and seconds, and units of declination are degrees, arcminutes, and arcseconds.

[a] Infrared luminosities are either taken from Farrah et al. (2003) or calculated using the formula in Sanders & Mirabel (1996) and converted to our cosmology. Units are the logarithm of the 1−1000 μm luminosity, in solar luminosities (3.826×10^{26} W).

[b] Observed-frame 1.4 GHz luminosities, computed from the National Radio Astronomy Observatory Very Large Array Sky Survey (NVSS) catalogs (Condon et al. 1998), in units of log W. The six objects without luminosities are not within the NVSS survey area.

[c] Astronomical Observing Request Key number.

[d] Redshift is taken from the *IRAS* Point Source Catalog Redshift Survey (PSCz; Saunders et al. 2000) rather than from Wilman et al. (1998), as our spectra are consistent with the PSCz redshift.

TABLE 2
Line Ratio Scaling Factors for Different Extinction Laws

Line Ratio	Fluks (1994)	Li & Draine (2001)	Draine (1989)	Chiar & Tielens (2006) ISM	Chiar & Tielens (2006) Galactic Center
[Ne III] λ15.56/[Ne II] λ12.81	1.075	1.052	1.120	0.881	0.734
[S III] λ18.71/[S III] λ33.48	0.684	0.775	0.634	...	0.360
[S IV] λ10.51/[S III] λ18.71	0.498	0.621	0.506	0.664	0.373
[S IV] λ10.51/[S III] λ33.48	0.340	0.478	0.321	...	0.134
[O IV] λ25.89/[Ne II] λ12.81	1.219	1.149	1.231	1.148	0.660
[Ne V] λ14.32/[Ne II] λ12.81	1.163	1.111	1.202	0.973	1.000
[Ne V] λ14.32/[Ne V] λ24.32	1.000	0.990	1.023	0.968	1.644

Note.—Scaling factors assume an increase in the V-band extinction of $A_V = 30$, in the form of a screen.

over a ~0.5 μm region centered on each line, and then fitting a single Gaussian profile to each line. We found a pure Gaussian profile to be a good fit to the lines in virtually all cases. The resulting 3 σ uncertainties in the wavelengths are themselves a function of wavelength, and are typically 0.01 μm at 10 μm, 0.03 μm at 20 μm, and 0.04 μm at 30 μm. Blended lines were measured by simultaneously fitting multiple Gaussians to the combined profile. Upper limits were determined by measuring the noise level of the data at the wavelength where the line is expected to lie; this can give rise to significant variations in upper limits for different lines in the same source if the wavelength of a line lies in an order overlap region.

2.3. *Extinction Corrections*

Previous authors have generally used either near-IR line ratios, or the [S III] λλ18.713,33.481 line ratio to derive an extinction correction (e.g., Verma et al. 2003); however, we only detect both [S III] lines in a small fraction of our sample, and the available near-IR spectroscopy for our sample is heterogeneous and incomplete. Given this, and the uncertain structure of the narrow-line-emitting gas in the mid-IR, we have chosen not to correct our line fluxes for extinction. We can, however, estimate what effect this lack of an extinction correction will have on our analysis. The relationship between the intrinsic and observed flux ratio for a pair of emission lines at wavelengths λ_1 and λ_2 can be written

$$\left(\frac{I_{\lambda_1}}{I_{\lambda_2}}\right)_{\rm int} = \left(\frac{I_{\lambda_1}}{I_{\lambda_2}}\right)_{\rm obs} \times 10^{0.4\left[(A_{\lambda_1}/A_V)-(A_{\lambda_2}/A_V)\right]A_V}, \qquad (1)$$

where A_{λ_1}, A_{λ_2}, and A_V are the extinctions at the wavelengths of the pair of lines and in the rest-frame V band, respectively. Assuming $A_V = 3.169 \times E(B-V)$, and obtaining values for $A_\lambda/E(B-V)$ from a standard extinction law (Li & Draine 2001) then allows us to estimate the effect on a line ratio in terms of an increase in the V-band extinction. Using this formalism, we find that the effect on most line ratios if A_V is increased is small. For example, for the [Ne III]/[Ne II] ratio we obtain

$$\left(\frac{[\text{Ne III}]}{[\text{Ne II}]}\right)_{\rm int} = \left(\frac{[\text{Ne III}]}{[\text{Ne II}]}\right)_{\rm obs} \times 10^{(-7.34\times10^{-4})A_V}, \qquad (2)$$

which is negligible unless the increase in A_V is at least a few tens. Hence our lack of an extinction correction, while important to be aware of, should not unduly affect our analysis of most line ratios, although the effect of a lack of an extinction correction on line luminosities is more significant. We discuss the effects of extinction in terms of an increase in A_V for both fine-structure line ratios and luminosities in the following sections.

Finally, we note that the magnitude, and in some cases the direction, of the effect on a line ratio for an increase in extinction depend significantly on ones choice of extinction law. In Table 2 we present the scaling factors for several line ratios for an increase in A_V, assuming some commonly used extinction laws. For a given line ratio there is broad consistency between the extinction laws, but differences of up to 25% between the scaling factors are common. These differences in scaling factors between extinction laws should be kept in mind in the following sections.

3. RESULTS

The SH spectra are presented in Figures 1–5, and the LH spectra are presented in Figures 6–10.

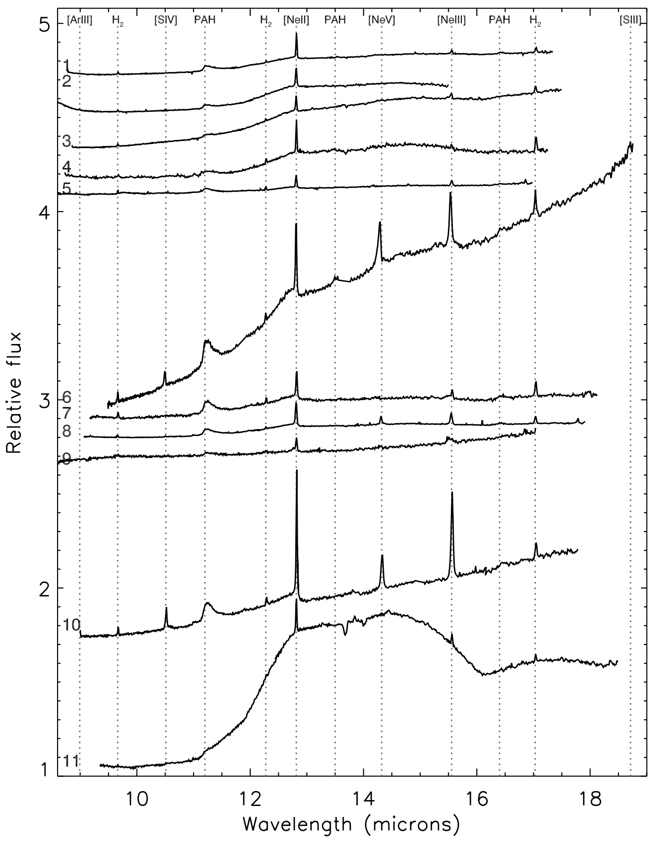

Fig. 1.—Short-High spectra of our sample. The numbers on the left-hand side correspond to the ID numbers in column one of Table 1. Wavelengths have been shifted to the (optical) rest-frame. Some objects also show absorption at 13.7 and 14.0 μm, caused by C_2H_2 and HCN gas (Lahuis et al. 2007).

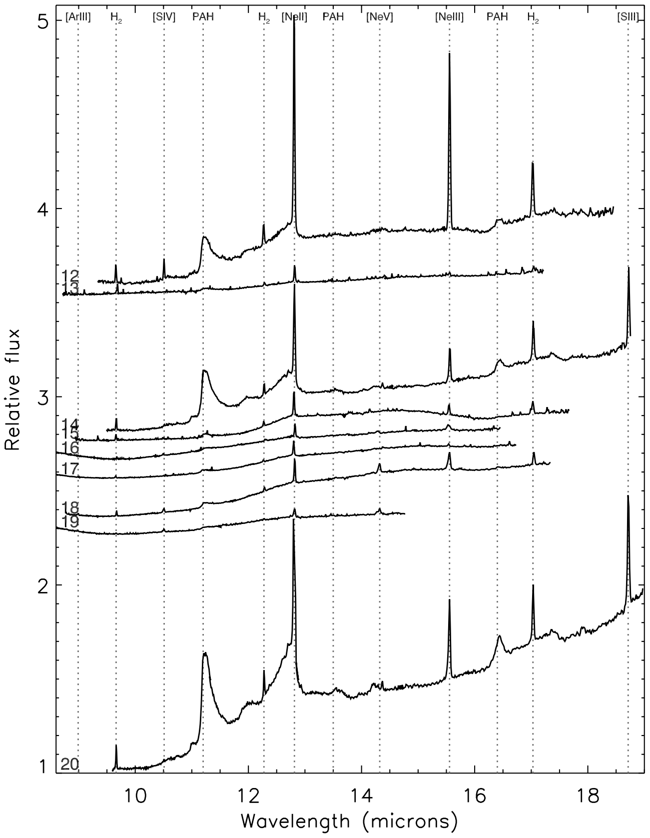

FIG. 2.—Short-High spectra (continued).

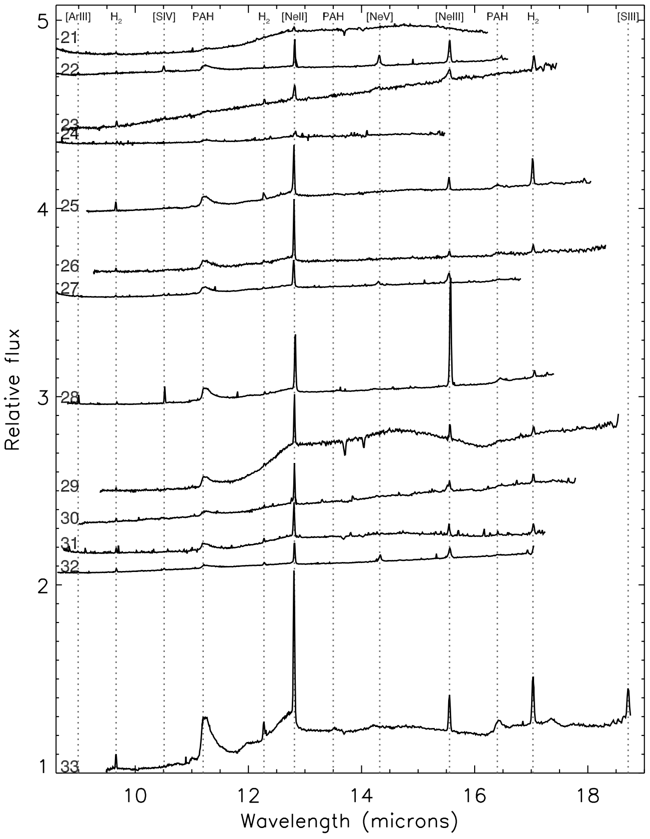

FIG. 3.—Short-High spectra (continued).

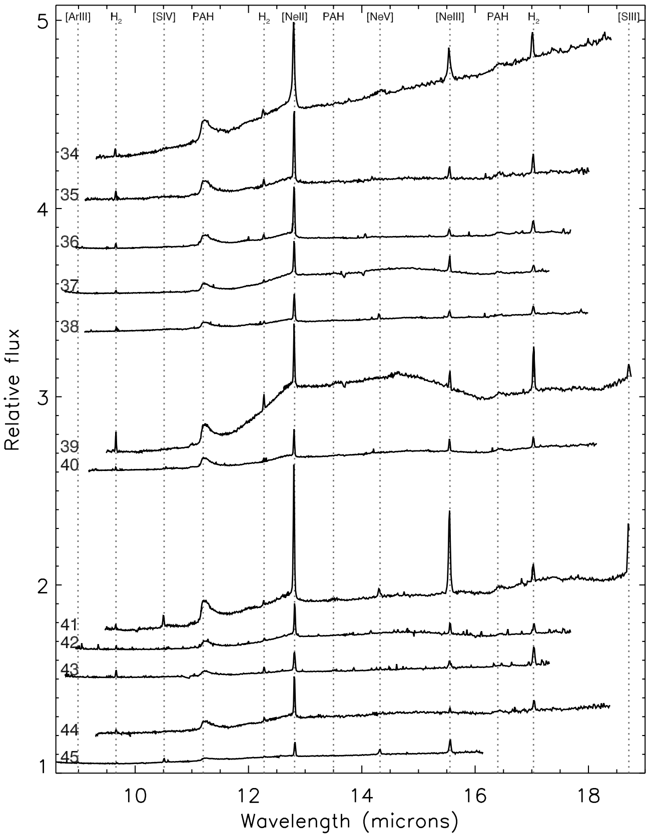

FIG. 4.—Short-High spectra (continued).

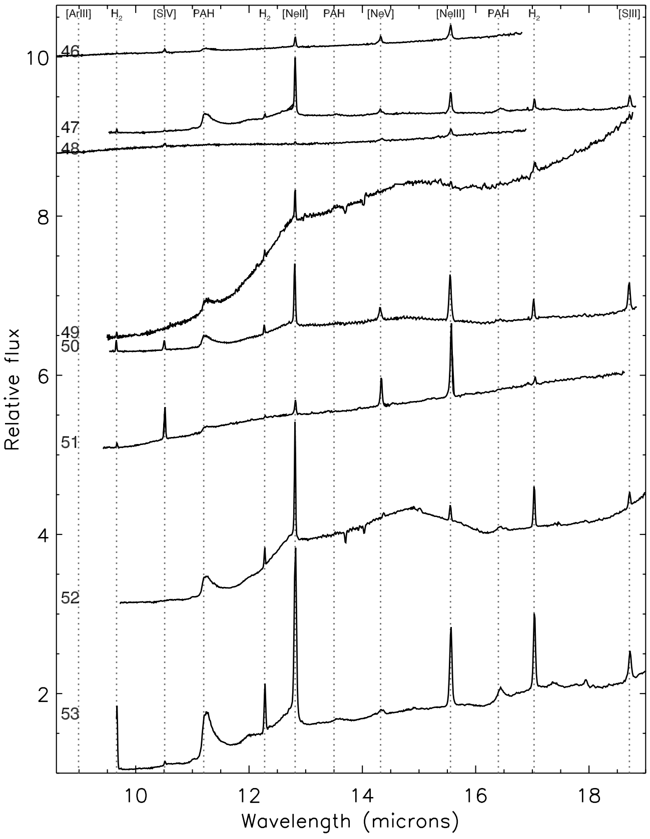

FIG. 5.—Short-High spectra (continued). Note different *y*-axis scaling.

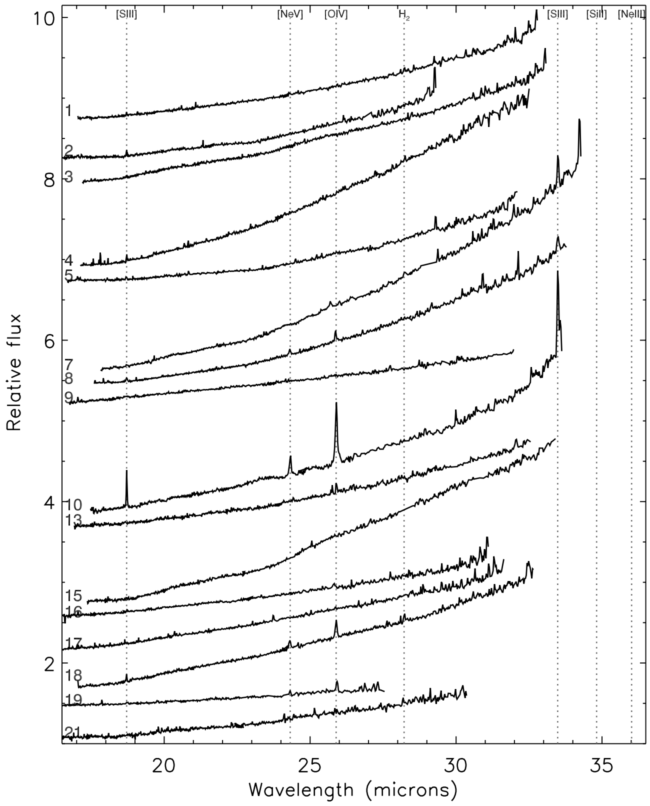

FIG. 6.—Long-High spectra of our sample. Note that the LH spectra are not arranged in order of ID number from Table 3 due to the wide dispersion in their continuum slopes. Wavelengths have been shifted to the (optical) rest-frame. Some objects also show an OH absorption feature at rest-frame 34.6 μm.

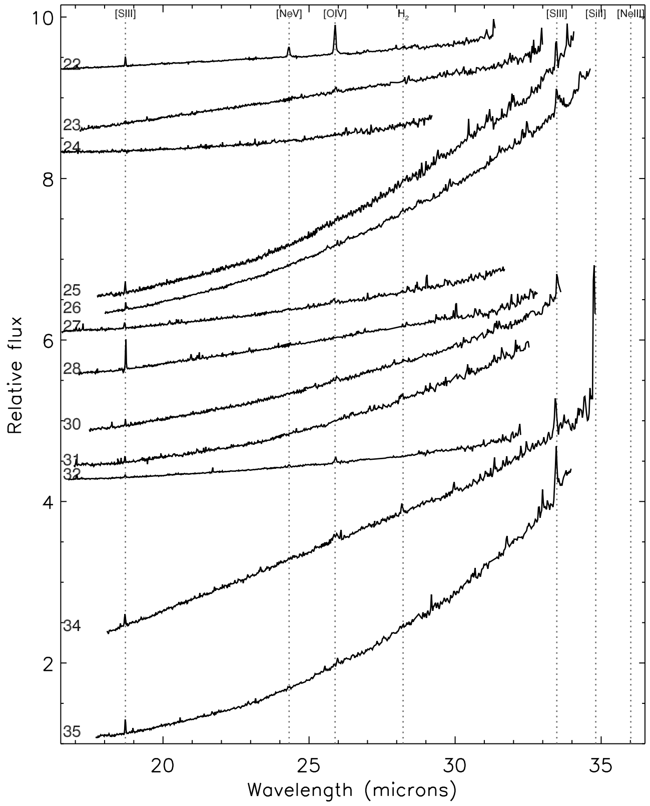

FIG. 7.—Long-High spectra (continued).

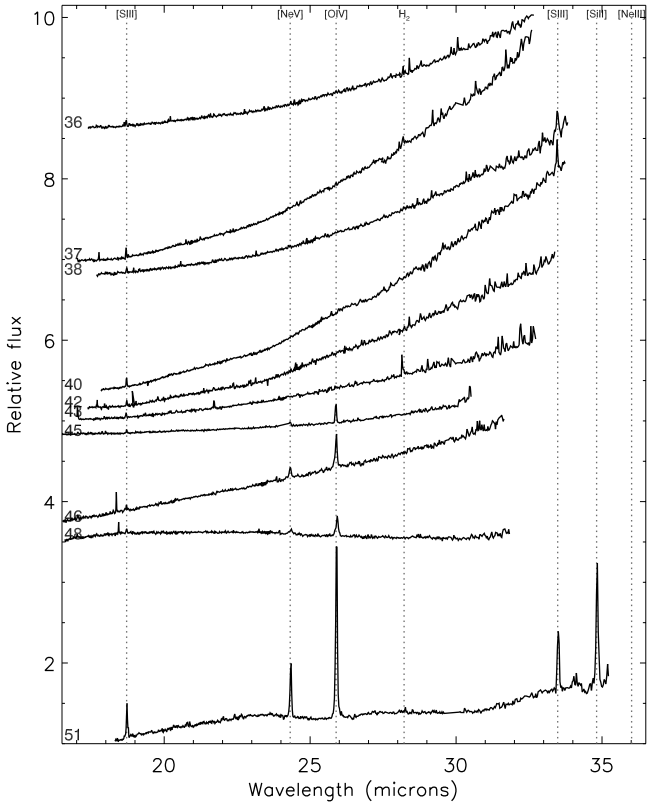

FIG. 8.—Long-High spectra (continued).

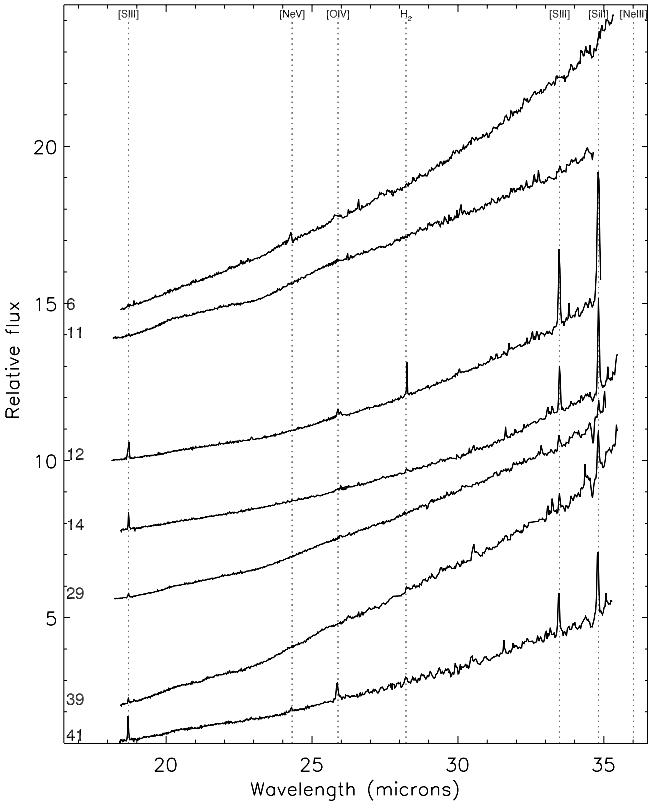

FIG. 9.—Long-High spectra (continued). Note that the *y*-axis scaling in this plot differs from that in Figs. 6–8.

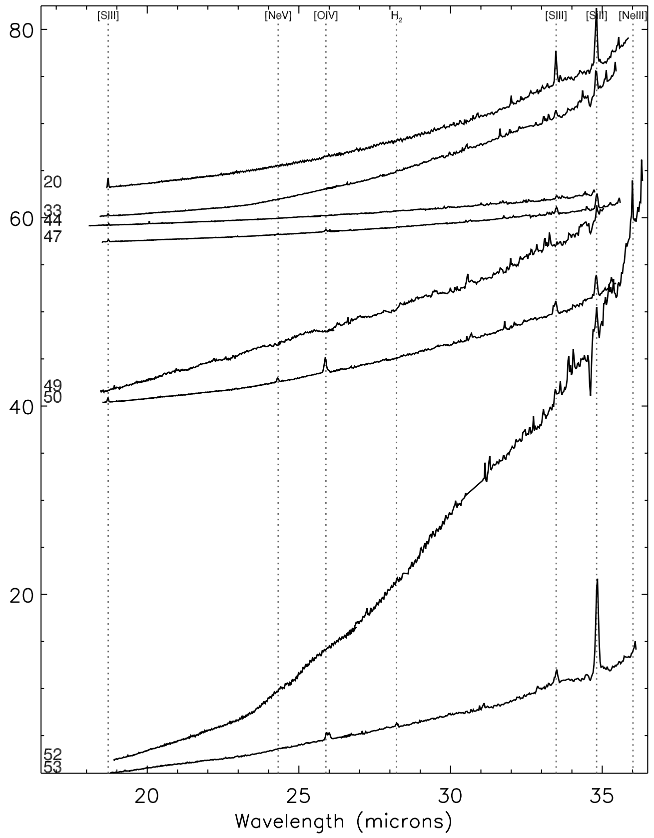

FIG. 10.—Long-High spectra (continued). Note that the y-axis scaling in this plot differs from that in Figs. 6–9.

3.1. *Common Lines*

All of the spectra show various fine-structure emission lines of neon, oxygen, sulfur, silicon, and (depending on redshift) argon. Also present are molecular hydrogen lines. These lines are listed in Table 3. We detect [Ne II] λ12.81 and [Ne III] λ15.56 in nearly every object. [S III] λ18.71 is also common, detected in ~80% of the sample, and [S IV] λ10.51 is detected in just under half of the sample. The detection of [S III] λ33.48 is dependent on redshift, requiring $z \lesssim 0.11$ (for the line to lie at <37 μm in the observed frame), but is detected in ~80% of the objects where this line lies within the LH bandpass. Other lines whose detection is dependent on redshift include [Ar II] λ8.99, which is detected in the majority of objects at $z \gtrsim 0.14$, and [S III] λ34.82, which is seen in about half of the objects at $z \lesssim 0.06$ (although this line lies in a noisy LH order even at $z = 0$ and thus is hard to detect). Three higher ionization lines are also present, although less commonly than the lines discussed above; [Ne V] λ14.32 and/or [O IV] λ25.89 are detected in just under half the sample, while [Ne V] λ24.32 is detected in about one-third of the sample. Turning to molecular hydrogen lines; the S(3), S(2), and S(1) pure rotational transitions of H_2 are seen in nearly all of the sample, while the S(0) H_2 transition is seen in about one-third of the sample, although its rarity compared to the other molecular hydrogen lines is probably as much to do with the rising continuum toward longer wavelengths as anything else. Our line fluxes are in all cases consistent with those in Armus et al. (2004, 2007) and Higdon et al. (2006), although we use a more recent version of the IRS pipeline. The fluxes reported here should therefore be more accurate than those previously published.

In addition to fine-structure (and other) emission features, some objects show one or more absorption features. The focus of this paper is the fine-structure emission lines, so here we only briefly mention these features, deferring a full discussion to later work. Several objects show two absorption features, corresponding to the vibration-rotation absorption bands of C_2H_2 at 13.70 μm and HCN at 14.02 μm. An extensive discussion of these features can be found in Lahuis et al. (2007). A total of 10 objects, most prominently Arp 220, IRAS 15250+3609 and IRAS 20551−4250, show an OH^- absorption feature at ~34.6 μm (IRAS 15250+3609 may also show a further OH^- absorption feature at rest-frame 28.9 μm, although the significance of detection is weak). This feature is most likely the ${}^2\Pi_{3/2}J = 3/2 - {}^2\Pi_{1/2}J = 5/2$ OH^- absorption doublet, which is thought to pump the 1612 MHz OH maser line (Elitzur et al. 1976). This absorption feature has been seen previously in Galactic sources (e.g., Justtanont et al. 1996), NGC 253 (Goicoechea et al. 2005), and Arp 220 (Skinner et al. 1997). The prominence of this feature in Arp 220 is consistent with the presence of an OH megamaser in this source (Lonsdale et al. 1994).

3.2. *Unusual Lines*

In addition to the lines discussed in the previous section, we also see a variety of "rare" (which we arbitrarily define as appearing in 10 or fewer objects) emission features in several objects, listed in Table 4. We detect [Cl II] λ14.37 in six objects, four of which also show [Ne V] λ14.32, leading to a double-peaked profile (see also Armus et al. 2006). In the other two objects only one peak is seen, and it is possible that we have confused [Cl II] λ14.37 with [Ne V] λ14.32; however, the velocity shift relative to the systemic (optical) redshift would have to be >5000 km s^{-1} for this to be the case. We therefore regard [Cl II] λ14.37 as the more likely identification. This line is seen in some lower luminosity starbursts (Spoon et al. 2000; Verma et al. 2003), but is rare in AGNs (Sturm et al. 2002). A number of low-ionization iron lines are present, including [Fe II] $\lambda\lambda$17.94, 24.52, 25.99 and [Fe III] λ22.93, all of which are seen (rarely) in lower luminosity starbursts and AGNs. We tentatively detect [P III] λ17.89 in two objects. This line is seen in small numbers of local IR-luminous sources, and in a variety of Galactic sources. Also present is the [Ar V] λ13.10 line, which is occasionally seen in AGNs (Sturm et al. 2002). One object, Arp 220, shows a weak detection of what is plausibly [Ne III] λ36.01, although Arp 220 is the only object in our sample at a low enough redshift for this line to enter a well-behaved part of the LH bandpass. We weakly detect the H I 7–6 line (i.e., the alpha transition of the Humphreys atomic hydrogen series) in four objects. Finally, two objects show features that appear to be real, but proved difficult to identify reliably, hence we have not listed them in Table 4. IRAS 23498+2423 shows a feature at a rest-frame wavelength of 10.581 μm with a flux of 3.17×10^{-22} W cm^{-2}. This feature is clearly resolved from the [S IV] λ10.511 line. If this feature is real, then possibilities include [Co II] λ10.521, which is seen in the 200–500 day mid-IR spectra of core collapse supernovae (Kotak et al. 2006), or [N III] λ10.682. IRAS 19297−0406 shows an emission feature with a flux of 3.88×10^{-21} W cm^{-2} that can plausibly be identified as the 31.77 μm water ice emission feature.

4. DISCUSSION

4.1. *Properties of the Narrow-Line Region Gas*

Mid-IR fine-structure lines can be used to study three properties of the narrow-line region (NLR) gas;[9] excitation, electron

---

[9] Due to *Spitzer*'s limited spatial resolution, the "NLR" of a ULIRG should be regarded as the ensemble of all the regions in a ULIRG where gas heated by star formation and/or an AGN emits fine-structure lines in the mid-IR.

TABLE 3

COMMON EMISSION LINES

Galaxy:	[Ar III]	H_2, $S(3)$	[S IV]	H_2, $S(2)$	[Ne II]	[Ne V]	[Ne III]	H_2, $S(1)$	[S III]	[Ne V]	[O IV]	H_2, $S(0)$	[S III]	[S III]
$\lambda_{\rm rest}$ (μm)	8.991	9.662	10.511	12.275	12.814	14.322	15.555	17.030	18.713	24.318	25.890	28.219	33.481	34.815
$E_{\rm ion}$ (eV)	27.6	...	34.8	...	21.6	97.1	41.0	...	23.3	97.1	54.9	...	23.3	8.2
00188−0856	<0.15	0.75	<0.26	0.32	4.67	<0.18	0.69	0.73	0.56::	<1.60	<0.90	1.39	...	...
00397−1312	0.35	0.32:	0.30	<0.27	4.41	<0.20	2.72:	1.09::	1.80:	<1.50	<1.20	<0.75	...	...
01003−2238	...	0.77	0.21	0.51:	3.14	<0.30	1.31	1.08	<0.90	<0.30	<0.30	<1.00	...	...
03158+4227	<0.60	<1.40	<1.20	0.89	5.78	<1.10	0.94::	2.86:	1.71:	<1.40	<1.80	<1.20	...	...
03521+0028	<0.42	0.80	<0.50	0.70	2.83	<0.45	1.27	1.94	0.87::	<0.48	<0.90	<0.51	...	...
05189−2524	...	3.22	5.63	1.67	21.12	17.53	17.76	3.15	3.18	11.73	23.71	<2.40	<24.00	11.85::
06035−7102	...	2.05	<0.39	1.20	6.98	<0.48	1.75:	2.71	3.00	<0.81	<3.00	2.25	4.61:	...
06206−6315	...	0.73	0.21	0.50:	6.58	2.30	2.86	1.36	2.06	2.03	3.00	<1.50	3.53	...
07598+6508	<0.60	<3.00	<0.66	0.78::	3.92	<0.75	2.45	1.79	<1.90	<3.00	<1.80	<3.20	...	...
08311−2459	...	2.41	8.70:	1.68:	24.29	12.34	22.53	2.80	11.43	9.81	26.30	<4.40	18.40:	...
08572+3915	...	0.43:	<0.50	<0.63	7.18	<0.75	1.99:	0.90	1.69::	<5.40	<6.00	<2.50	<12.00	<25.00
09022−3615	...	6.32	5.05	6.02	56.58	<2.40	40.00	10.81	24.73	<3.60	6.72	11.16	41.33	95.83
10378+1109	<2.00	1.10	<0.41	0.85	3.51	<1.10	0.60::	0.55::	<3.90	<2.40	2.03::	<2.70	...	...
10565+2448	...	4.05	<0.27	2.53	64.06	<1.00	7.57	6.42	13.23	<0.90	<1.20	1.85::	23.92	43.40
11095−0238	...	1.80	<1.20	1.19	6.08	<0.48	1.89	2.63:	1.22:	<1.80	<0.90	<4.00	...	...
11119+3257	<0.30	0.52	<1.50	0.47::	2.97	0.75	1.98	<2.60	<1.80	<0.90	1.88::	<1.50	...	...
12018+1941	<0.20	0.55:	<0.19	0.60:	3.00	<0.80	0.35	<1.80	<0.70	<0.10	<0.63	2.67:	...	...
12071−0444	0.61	1.36	1.46	0.85	5.25	2.88	5.09	2.12	1.86:	3.71	6.55	<2.00	...	...
12514+1027	0.68	0.27::	0.91	0.50	2.35	1.94	2.68:	1.14::	1.21::	1.67:	2.71:	...	...	...
13120−5453	...	6.89	0.50:	5.50	150.04	1.71	18.46	9.49	19.18	<20.00	6.42:	<5.00	60.64	107.13
13218+0552	<0.09	0.44:	<0.20	0.25:	1.07:	<0.25	<0.85	0.98:	<1.60	<3.40	<2.40	<4.00	...	...
13342+3932	0.73	0.40::	2.12	0.35	5.69	3.45	4.97	1.20	2.97	4.23	10.32	0.72:	...	...
13451+1232	0.51	1.82	0.69::	1.19	5.03:	1.02:	5.11	2.46	1.23:	<2.1	2.14:	1.23::	...	...
14070+0525	<0.27	0.58	<0.20	0.29::	1.84:	<0.15	0.58:	0.56:	<0.66	<0.60	<1.50	<1.10	...	...
14348−1447	...	2.87	0.25::	1.86	10.76	<0.21	2.59	4.97:	4.09:	<1.50	<3.30	<4.20	3.79:	...
14378−3651	...	0.95	<0.60	1.25	11.39	<0.90	1.20	1.39	2.50	<2.30	<3.80	<2.90	5.74:	<25.00
15001+1433	0.44:	0.60	0.42:	0.37:	6.85	1.12	2.61	1.50:	2.25	0.66::	1.75	<1.10	...	...
15206+3342	2.10	0.54	4.35	0.35:	13.29	<0.4	20.52	1.06:	8.63	<1.50	<2.40	<2.00	...	...
15250+3609	...	0.74	<0.69	0.60:	10.05	<1.20	2.68	1.17	4.27	<2.40	<1.50	<1.20	6.75:	<19.00
15462−0450	...	0.97	<0.25	0.41:	7.38	<0.30	1.38:	1.45	1.78:	<1.05	<3.60	<2.00	4.80:	...
16090−0139	0.68:	1.52	<0.20	0.79	7.76	<0.12	1.98:	1.85	1.83:	<2.00	<1.40	<3.00	...	...
17179+5444	0.44:	1.16	0.46	0.78	4.54	2.21	2.90	2.01:	1.35:	0.82	2.10	<0.24	...	...
17208−0014	...	5.45	<0.40	6.06	41.22	<1.00	8.12	9.75	7.29	<3.20	<2.40	3.41:	17.80	38.87:
19254−7245	...	3.05	<1.20	1.82	31.48	2.77:	13.19	6.14	4.28	<1.60	6.35:	2.63:	9.07	56.80::
19297−0406	...	2.54	<0.39	1.71	17.69	<0.92	2.46	3.38	4.93:	<2.20	<0.90	<6.00	9.15:	...
20087−0308	...	1.59	<0.48	1.14	14.14	<0.75	1.64	2.63	2.62	<1.90	<1.60	<2.10	17.73	...
20100−4156	0.46:	1.03	<0.20	0.60	7.26	<0.48	2.78:	1.19	2.74	<1.30	<4.80	1.82:	...	...
20414−1651	...	1.44	<0.36	0.55:	6.85	1.00	1.57	1.60	2.16	<1.50	<1.80	<2.00	7.99	...
20551−4250	...	5.66	<0.39	3.36	13.01	<0.75	2.79	7.93	4.26	<1.50	<2.00	5.05:	<10.00	22.29
22491−1808	...	0.92	<0.40	0.87	5.37	<0.45	1.85	1.67	2.69	<0.90	<2.40	<4.50	4.75:	...
23128−5919	...	1.55	4.43	1.02	27.29	2.56	20.44	3.12	23.34	2.96:	18.16	<12.00	22.47	17.48
23230−6926	...	0.93	<0.70	0.54	7.38	<0.75	1.96	2.08	1.77	<1.20	<1.50	<3.00	<24.00	...
23253−5415	<2.10	2.45	1.08	1.30	5.47	0.33::	1.87	3.68	1.66	1.21	1.20::	2.14::	...	...
23365+3604	...	1.42	<0.75	1.01:	8.57	<0.80	0.73	2.11	3.01:	<0.54	<2.00	<6.20	3.81::	41.64::
23498+2423	0.31:	0.44:	1.14:	0.21	3.17	1.15	2.71	0.85:	1.66:	2.01	5.00	0.53	...	...
Mrk 1014	0.69	0.67	3.69	0.30	6.57	7.40	9.71	1.15:	<1.50	4.96	12.97	1.61	...	...
UGC 5101	...	2.48	0.91:	2.40	34.13	2.57	13.66	4.59	5.57	2.82:	7.35	1.17	15.46	32.07
3C 273	<1.50	<0.75	3.04:	<0.80	1.55	3.38	6.00	1.21:	1.53	2.94	8.47	<2.40	...	...
Mrk 231	...	3.56	<2.10	4.24:	19.67	<3.0	3.05:	9.17	<4.00	<18.00	<9.50	<20.00	<8.00	16.00::
Mrk 273	...	9.38	9.58	5.21	41.90	11.68	33.57	8.63	13.35	15.38	56.36	<9.00	42.56	14.66:
Mrk 463	...	3.89	29.86	1.19	9.25	18.25	40.78	3.48	15.85	19.93	69.17	0.95::	15.50	29.79
Arp 220	...	...	<1.50	10.06	64.54	<2.9	7.80	19.15	5.44	<14.00	<21.00	<26.00	75.08::	32.28
NGC 6240	...	65.63	2.68	34.95	171.22	4.40	60.65	44.29	17.13	<5.70	26.75	6.21:	38.11	265.86

NOTES.—Flux units are $\times 10^{-21}$ W cm^{-2}. Ellipses indicate that the line is outside the bandpass. Errors are of the order 10% or less, except for those fluxes marked with a ":," which are 20% and those marked with a "::," which are 30% and should be considered suspect.

TABLE 4

Unusual Emission Lines

Galaxy:	H i 7–6	[Ar v]	[Cl ii]	[P iii]	[Fe ii]	[Fe iii]	[Fe ii]	[Fe ii]	[Ne iii]
$\lambda_{\rm rest}$ (μm)	12.368	13.102	14.365	17.885|	17.936	22.925	24.519	25.988	36.014
$E_{\rm ion}$ (eV)	7.9	59.8	109.2	13.0	19.8	7.9	16.2	7.9	41.0
01003−2238	...	0.46	...	...	...	...	...	...	...
03521+0028	...	...	...	...	...	...	0.88	...	...
09022−3615	...	...	...	...	...	...	...	5.28:	...
10565+2448	...	...	0.99	...	...	...	...	1.69:	...
12018+1941	...	...	0.30::	...	...	...	...	...	...
12514+1027	...	...	...	1.35::	...	...	...	...	...
13120−5453	0.75::	...	...	...	...	...	...	5.37	...
14070+0525	0.43:	...	...	...	...	...	...	...	...
15206+3342	0.23:	...	...	...	...	1.00	...	...	...
17208−0014	...	...	...	...	...	...	...	2.80::	...
19297−0406	...	...	...	...	...	...	...	1.70	...
20100−4156	0.28:	...	...	...	...	...	...	...	...
23498+2423	...	...	0.70	0.70:	...	...	...	...	...
Mrk 463	...	0.97	...	...	...	...	...	...	...
UGC 5101	...	...	0.79:	...	...	...	...	3.14::	...
NGC 6240	...	...	2.38	...	5.49	...	...	21.62	...
Arp 220	...	...	2.51	...	...	...	...	...	48.03::
Mrk 231	...	...	...	...	...	...	...	...	...

Notes.—Flux units are $\times 10^{-21}$ W cm^{-2}. In this table, ellipses indicate that the line is not seen, however, we do not quote upper limits due to the uncertain nature of the line IDs. Formal errors are all of the order 10%, except for ":," which are 20%, and "::," which are 30%.

temperature, and electron density. Measuring electron temperature though requires combining a mid-IR line with an optical or near-IR line of the same species. In this paper, we therefore concentrate only on electron density and excitation.

4.1.1. *Electron Density*

The electron density in a NLR can be estimated by using the ratios of two lines representing transitions from the same orbital and suborbital (i.e., the same principal and angular momentum quantum numbers), but with different numbers of electrons in that (sub)orbital. For our sample there are two line ratios that satisfy this requirement; the $^3p_2 -^3 p_1$ and $^3p_1 -^3 p_0$ transitions of [Ne v] at 14.32 and 24.32 μm, and the $^3p_2 -^3 p_1$ and $^3p_1 -^3 p_0$ transitions of [S iii] at 18.71 and 33.48 μm. These ratios can then be converted to an electron density by solving the relevant rate equation. Of the two, the [Ne v] ratio is more useful. Its high-ionization potential of 97 eV means that it can only be produced (at a level observable in a ULIRG) by an AGN, making it more straightforward to interpret than the [S iii] ratio. Furthermore, for most extinction laws the extinctions of the two [Ne v] lines are virtually identical (Table 2; see also Draine 2003), making the [Ne v] ratio only marginally sensitive to the lack of an extinction correction.

Sixteen of the ULIRGs in our sample show detections in both [Ne v] lines. The line ratios for these objects span the range $0.57 <$ [Ne v] λ14.32/[Ne v] λ24.32 < 2.69, with a fairly even spread. The nine objects that are only detected in [Ne v] λ14.32 have lower limits on the [Ne v] line ratio consistent with this range. Using Figure 3 of Alexander et al. (1999), then, these [Ne v] line ratios are consistent with electron densities of $<10^4$ cm^{-3} in all cases, well below the critical densities of the two lines. Our derived electron densities are also comparable to those derived (using the same [Ne v] ratio) for lower luminosity AGNs (Sturm et al. 2002). As a check, we examine the [S iii] line ratio; for those objects with detections in both lines we see a range of $0.14 <$ [S iii] λ18.71/[S iii] λ33.48 < 1.10, consistent with electron densities of $\lesssim 10^{3.5}$ cm^{-3}. It is important to note, however, that we expect the [Ne v] and [S iii] line ratios to give different electron densities, because the [Ne v] lines are likely produced solely by the AGN, while the [S iii] lines (probably) arise from both starburst- and AGN-heated regions.

4.1.2. *Excitation*

If electron densities are below the critical density, then the excitation level of the NLR can be estimated by considering flux ratios of adjacent ionization states of the same element, e.g., for an element X; $f_{{\rm X}^{i+1}}/f_{{\rm X}^i}$. For a fixed number of ionizing photons per hydrogen atom (i.e., a given ionization parameter U), this ratio will be approximately proportional to the number of photons producing the observed X^i flux relative to the number of Lyman continuum photons, although if U varies then $f_{{\rm X}^{i+1}}/f_{{\rm X}^i}$ will also vary. Therefore, for a fixed U, a higher value of $f_{{\rm X}^{i+1}}/f_{{\rm X}^i}$ indicates a harder radiation field, although the details depend on the element in question.

Our spectra contain a limited number of lines, hence detailed excitation diagnostics are not possible. We can, however, get a qualitative idea of the range in excitations in our sample. The two most useful diagnostic ratios are [Ne iii] λ15.56/[Ne ii] λ12.81 and [S iv] λ10.51/[S iii] λ18.71. Both neon and sulfur are abundant in Galactic sources, with both [Ne/H] and [S/H] lying approximately in the range 10^{-4}–10^{-6}. Furthermore, the photon energies required to produce any of these four ions are $<$50 eV, meaning that they can all be produced in star-forming regions as well as AGNs. All four lines are seen in Wolf-Rayet star spectra (Smith & Houck 2001), H ii regions (Peeters et al. 2002), planetary nebulae (Bernard-Salas et al. 2001), as well as the integrated spectra of local galaxies. We might also expect [Ne iii] and [S iv] to increase in strength relative to [Ne ii] and [S iii] in lower density and/or lower metallicity star-forming regions (Thornley et al. 2000; Ho & Keto 2007). It is, however, strange, given their similar ionization energies, that we detect [Ne iii] λ15.56 in virtually all the sample, but only detect [S iv] λ10.51 in about 45% of the

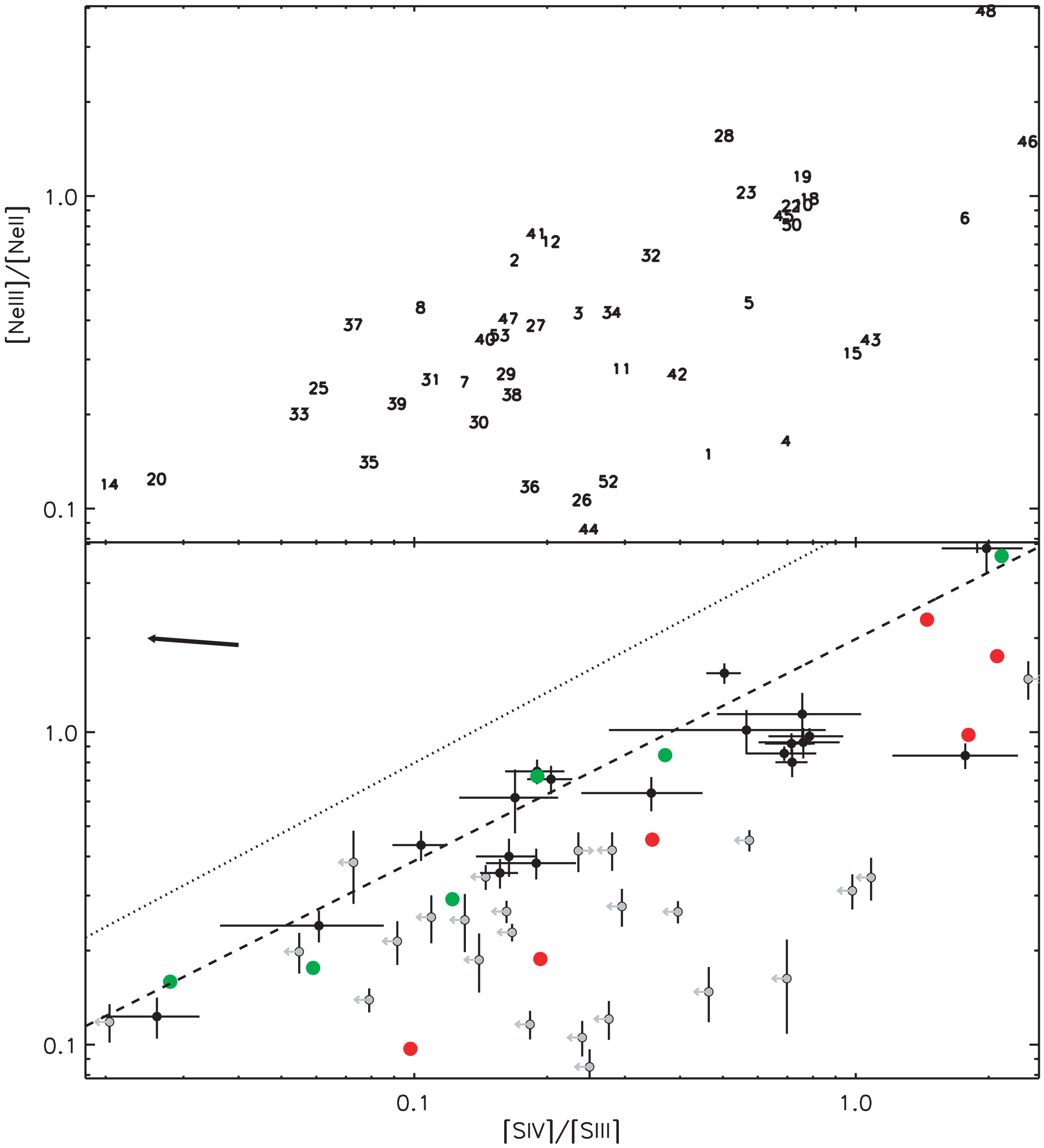

Fig. 11.—Excitation diagnostic. The top panel identifies the ULIRGs using the numbers in the first column of Table 1, while the bottom panel shows the ULIRGs with error bars and 3 σ limits, as well as ancillary data. ULIRGs with detections on both axes are plotted in black, while ULIRGs with limits on one or both axes are plotted in gray. Green symbols represent starbursts (Verma et al. 2003), and red symbols represent AGNs (Sturm et al. 2002), both with IR luminosities approximately in the range 10^{10}–$10^{11.5}$ $L_\odot$. The dotted line shows the fit to star-forming galaxies, while the dashed line shows a fit to Seyfert galaxies, both with IR luminosities of $\lesssim 10^{10}$ $L_\odot$ (Dale et al. 2006). The arrow indicates the effect on a points position if the V-band extinction is increased by $A_V = 30$ (but see Table 2).

sample. The [S IV] λ10.51 line lies close to the 9.7 μm silicate feature, but we detect the H_2, $S(3)$ λ9.66 line in most of our sample, in many cases with a flux that is lower than the upper limit on the [S IV] λ10.51 line. The most likely explanation for this is that the neon- and sulfur-emitting zones in ULIRGs lie within regions extincted by silicate dust, while the H_2-emitting region lies outside it (see also Higdon et al. 2006). This is supported by the fact that we do not detect [S IV] λ10.51 in any object that has a silicate strength (Levenson et al. 2007) greater than 2.1 (see Spoon et al. [2007, in preparation] for the silicate strengths of our sample).

In Figure 11 we plot an "excitation plane" of [Ne III]/[Ne II] versus [S IV]/[S III] for our sample. The ULIRGs span a broad range in excitation, but with a positive correlation between the sulfur and neon line ratios, suggesting that we are seeing emission from the same region in both species. A similar correlation has previously been noted for blue compact dwarf galaxies (Wu et al. 2006), and for nearby infrared-faint galaxies (Dale et al. 2006). The ULIRGs are fairly evenly distributed across the correlation region, with no obvious over or underpopulated regions.

Also plotted in Figure 11 are data for starbursts and AGNs with IR luminosities (mostly) between 1×10^{10} and 3×10^{11} $L_\odot$ (Verma et al. 2003; Sturm et al. 2002), and the relations from Figure 4 of Dale et al. (2006) for star-forming regions and IR-faint AGNs, the bulk of which have IR luminosities below 1×10^{10} $L_\odot$. The ULIRGs occupy the same region in the ionization plane as the Verma et al. (2003) and Sturm et al. (2002) starburst and AGN samples. Barring some particularly subtle bias from a lack of extinction correction, this suggests that the mid-IR–emitting narrow-line region gas in ULIRGs is excited in broadly the same way as the NLR in $10^{10} \lesssim L_{\rm IR}(L_\odot) \lesssim 3 \times 10^{11}$ starbursts and AGNs, and that any differences in density, metallicity, or star formation history between ULIRGs and lower luminosity systems are

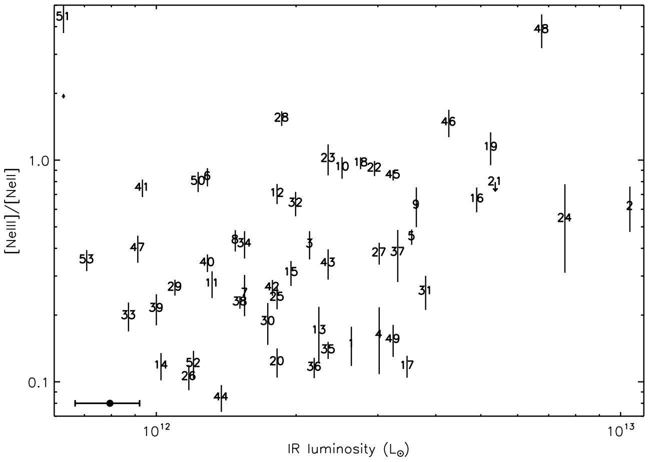

FIG. 12.—[Ne III] λ15.55/[Ne II] λ12.81 vs. infrared luminosity. The small arrow indicates the effect on a points position if the *V*-band extinction is increased by $A_V = 30$. The horizontal bar on the bottom left indicates a 20% error on the IR luminosity.

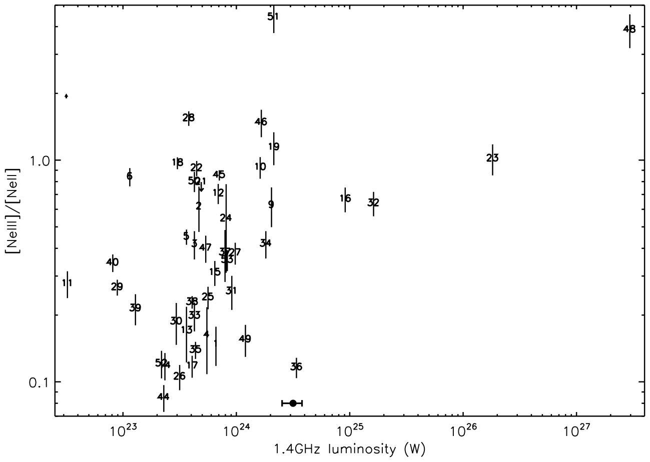

FIG. 13.—[Ne III] λ15.55/[Ne II] λ12.81 vs. 1.4 GHz luminosity. The small arrow indicates the effect on a points position if the *V*-band extinction is increased by $A_V = 30$. The horizontal bar on the bottom left indicates a 10% error on the 1.4 GHz luminosity.

not sufficient to manifest themselves in simple ionization plane diagrams.

The same does not, however, appear to be true for systems with $L_{\rm IR} \lesssim 10^{10}$ $L_\odot$. The ULIRGs are consistent with the slopes of the Dale et al. (2006) relations, but are offset below them by ~0.2 dex. Increased extinction in the form of a foreground screen could explain this, but would require an additional $A_V \simeq 60$ of foreground extinction (and see also Table 2). An (arguably) more likely explanation is that there is a decrease in the intrinsic [Ne III]/[Ne II] ratio for a given [S IV]/[S III] ratio in going from $L_{\rm IR} \simeq 10^{10}$ $L_\odot$ starbursts to $L_{\rm IR} \simeq 10^{12}$ $L_\odot$ systems. It is beyond the scope of this paper to investigate this effect in detail, so here we simply suggest a possible explanation. From Table 3, [S IV] has a significantly smaller ionization energy than [Ne III], and the difference in ionization energies between [S IV] and [S III] is smaller than the difference between [Ne III] and [Ne II]. This means that if we increase the gas density in the NLR or decrease the hardness of the ionizing radiation, then both the [Ne III]/[Ne II] and [S IV]/[S III] ratios will decrease, but the [Ne III]/[Ne II] ratio will decrease by a larger fraction than the [S IV]/[S III] ratio. As we might expect the gas density in the NLR of ULIRGs to be significantly higher than in $L_{\rm IR} \lesssim 10^{10}$ $L_\odot$ star-forming regions, we might also expect a smaller [Ne III]/[Ne II] ratio in ULIRGs for a given [S IV]/[S III] ratio than in lower luminosity starbursts. A softer ionizing radiation field in ULIRGs compared to lower luminosity starbursts would produce a similar effect.

We can also explore variations in excitation as a function of the total emission. In Figure 12 we plot the [Ne III]/[Ne II] ratio against infrared (rest-frame 1–1000 μm) luminosity. There is no discernible correlation. Two ULIRGs, Mrk 463E and 3C 273, have elevated [Ne III]/[Ne II] ratios (although with very different IR luminosities), while the rest of the sample is confined to [Ne III]/[Ne II] ratios in the range 0.08–1.05, irrespective of their IR luminosity. This picture remains broadly the same if we substitute IR luminosity for radio luminosity (Fig. 13). In this case, objects with 1.4 GHz luminosities lower than ~$10^{24.5}$W show no discernible correlation between radio luminosity and [Ne III]/[Ne II] ratio. Those objects with higher radio luminosities appear to be confined to higher [Ne III]/[Ne II] ratios, and with a narrower spread, although the number of objects with $L_{1.4} > 10^{24.5}$ W is too small to draw firm conclusions. We conclude therefore that neither 1–1000 μm luminosity or 1.4 GHz luminosity are good proxies for the excitation of the NLR in ULIRGs.

4.2. *Starburst and AGN Activity*

Mid-IR emission from galaxies can arise from five sources: (1) a nonthermal component, e.g., supernova remnants; (2) photospheres of evolved stars; (3) ionized gas; (4) dust grains; and (5) molecular gas. In most ULIRGs the latter three sources dominate the mid-IR emission. The ionized gas gives rise to the fine-structure lines, while the smaller dust grains produce the mid-IR continuum longward of about 10 μm. Larger dust grains give rise to features such as the absorption features at 9.7 and 18 μm (Lebofsky & Rieke 1979; Roche & Aitken 1985; Chiar & Tielens 2006). Large molecules give rise to several emission and absorption features; the most prominent emission features are seen from 3.3 to about 19 μm and arise from bending and stretching modes of polycyclic aromatic hydrocarbons (Puget & Leger 1989; Hony et al. 2001). Other molecular features include several hydrogen emission lines, as well as weaker features such as CO, HCN, and C_2H_2 gas absorption (Spoon et al. 2006; Bernard-Salas et al. 2006; Lahuis et al. 2007).

The use of these mid-IR emission and absorption features as diagnostics of the power source in ULIRGs is, however, not straightforward. The fundamental problem is that dust and gas simply require a source of ionizing radiation to emit in the mid-IR, and do not particularly care what the source of that ionizing radiation is. In principle, a population of hot stars or an accretion disk around a supermassive black hole both serve equally well. Exhaustive reviews of these difficulties are given elsewhere (e.g., Lonsdale et al. 2006; Dale et al. 2006), so here we highlight some examples. Fine-structure line fluxes are affected by several factors, particularly in starbursts, where the age of the burst, the geometry of the region and the upper and lower bounds on the initial mass function (IMF) can all have a drastic effect on observed line ratios (e.g., Fig. 6 of Thornley et al. 2000). The factors determining PAH strengths are still poorly understood; one factor that is known to have a significant effect is metallicity, with strong suppression of PAHs seen in low-metallicity environments (Roche et al. 1991; Thuan et al. 1999; Dwek 2005; Wu et al. 2006). There is also no a priori reason why PAH bending and stretching modes cannot be excited by an AGN, although observationally PAHs seem to be almost exclusively associated with either star-forming regions or ambient interstellar light (Peeters et al. 2004). Significant silicate absorption on the other hand merely requires a mass of warm dust obscured by a significant column of cooler dust, and

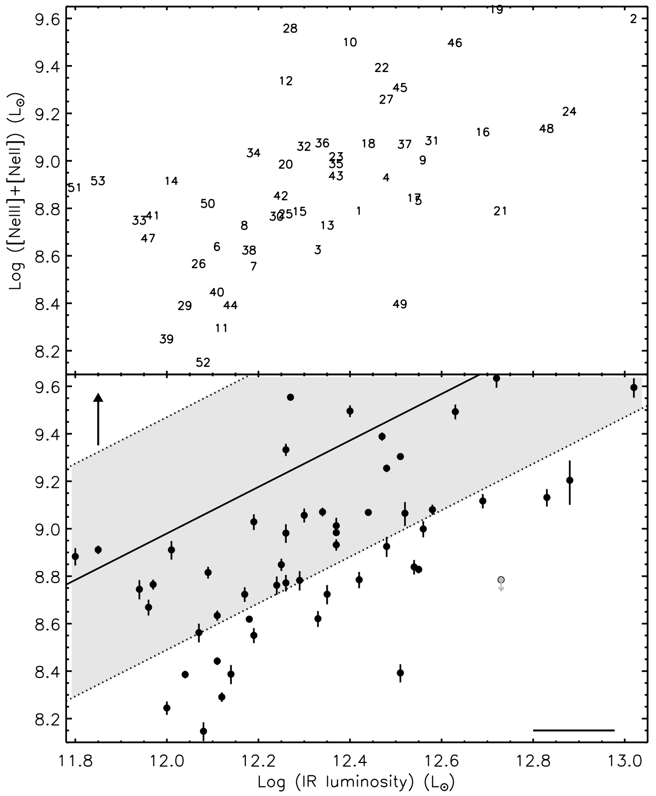

FIG. 14.—Total luminosity of the [Ne III] $\lambda 15.55$ and [Ne II] $\lambda 12.81$ lines vs. IR luminosity. The solid line is the relation in Ho & Keto (2007), and the dashed lines indicate their 1 σ errors. ULIRGs with detections on both axes are plotted in black, while ULIRGs with limits on one or both axes are plotted in gray. The arrow indicates the effect on a points position if the *V*-band extinction is decreased by $A_V = 30$. The horizontal bar on the bottom left indicates a 20% error on the IR luminosity.

therefore on its own says nothing about what is heating the warm dust.

With these subtleties in mind, we examine the nature of the starburst and AGN activity in our sample. We focus here on a limited number of diagnostics, deferring detailed analysis to upcoming papers.

4.2.1. *Neon Lines and Star Formation*

Recently, Ho & Keto (2007) have suggested that the total luminosity of the [Ne II] $\lambda 12.81$ and [Ne III] $\lambda 15.56$ lines are a diagnostic of star formation rates in galaxies across a wide range in IR luminosity. This method potentially offers a number of advantages over other mid-IR star formation diagnostics; the neon lines in question are strong and easily observed, and the dependence on an accurate extinction correction is small. With ULIRGs, however, there is the obvious caveat that some or all of the [Ne II] $\lambda 12.81$ and [Ne III] $\lambda 15.56$ may originate in regions excited by an AGN rather than a starburst, so in this section we explore the use of the [Ne II] $\lambda 12.81$ and [Ne III] $\lambda 15.56$ lines as star formation rate diagnostics in our sample.

In Figure 14 we plot the [Ne III] + [Ne II] luminosities of our sample against total IR luminosity, and overplot the relation given in equation (2) of Ho & Keto (2007). There is a large scatter in the [Ne III] + [Ne II] luminosities as a function of IR luminosity for our sample, comparable to the scatter seen in Figure 1 of Ho & Keto (2007), but we see a clear upward trend in [Ne III] + [Ne II] luminosity with increasing IR luminosity. A power-law fit yields $L_N \propto L_{\rm IR}^{0.75}$, and a horizontal line fit (i.e., no dependence of [Ne III] + [Ne II] luminosity on IR luminosity) is ruled out at $>5\,\sigma$ significance. The slope of the relation for the ULIRGs is consistent with the slope of the Ho & Keto relation plotted in Figure 14, but the ULIRGs are systematically lower, offset by $\sim$0.4 dex, on average. There are several possible explanations for this offset. First is that an AGN is contributing to the total IR luminosity but not to the neon line fluxes; however, this explanation seems unlikely, as we see systems with known IR-luminous AGNs scattered on either side of the Ho & Keto line; Mrk 463E and NGC 6240 both lie above it, whereas Mrk 231 and IRAS 03158+4227 (which contains a Compton-thick AGN; Risaliti et al. 2000) both lie well below it. Second is a different electron density in the NLR of ULIRGs, either significantly lower than that seen in lower luminosity starbursts, or much higher and approaching the critical density. A high electron density, however, is ruled out (see § 4.1.1), and there is no evidence for electron densities substantially lower than in lower luminosity systems. A significantly lower metallicity would also serve to lower neon luminosities for a given IR luminosity, but again there is no evidence (or indeed plausible motivation) for such low metallicities in local ULIRGs. Finally, this offset could be caused by higher extinction. This explanation seems the most likely. Although the Ho & Keto relation was derived without correcting for extinction, we expect ULIRGs to suffer heavier extinction in their nuclear regions relative to lower luminosity starbursts. The offset seen for ULIRGs corresponds to $A_V = 40 \pm 20$ over and above the extinction seen in lower luminosity systems.

4.2.2. *PAHs and Star Formation*

The correlation between [Ne III] $\lambda 15.56$ + [Ne II] $\lambda 12.81$ luminosity and IR luminosity is consistent with the idea that there is a correlation between [Ne III] $\lambda 15.56$ + [Ne II] $\lambda 12.81$ luminosity and star formation rate in ULIRGs. This on its own, however, does not support such a hypothesis, as we expect the luminosity of any mid-IR fine-structure line to correlate approximately with the mid-IR luminosity of the ionizing source, irrespective of what that source may be. Therefore, to test this hypothesis further, we examine the relationship between [Ne III] $\lambda 15.56$ + [Ne II] $\lambda 12.81$ luminosity and the luminosity of PAH features.

The origin of PAH features and their use as star formation indicators are still controversial (e.g., Peeters et al. 2004; Förster Schreiber et al. 2004). Observationally, however, PAH features are usually prominent in starburst galaxies, with previous authors noting a good correlation between the strength of PAH features and IR luminosity in starbursts (Brandl et al. 2006), but appear to be weak or absent in AGNs (Weedman et al. 2005). The cause of this dichotomy is thought to be a combination of two factors. First, the UV radiation field from an accretion disk around a black hole is harder than the UV radiation field from a starburst, and is therefore more adept at destroying the C—H and C—C bonds in PAHs. Second, a luminous AGN produces a prominent mid-IR continuum that can drown out PAH features, even if there is a vigorous starburst present (Laurent et al. 2000).

Even though there is good evidence that PAHs originate in star-forming regions, the behavior of individual PAH features as a function of star formation rate remains uncertain, with strong variations observed in individual PAH feature strengths between different starburst galaxies (Smith et al. 2007). Therefore, we elect to use the combined luminosities of two PAH features in order to reduce the likely scatter introduced by variances in individual PAH strengths. The choice of the two PAH features is a straightforward one; the most luminous PAH features are those at 6.2, 7.7, and 11.2 μm, but the 7.7 μm feature is difficult to measure as it lies in a crowded part of the spectrum. Therefore, even though

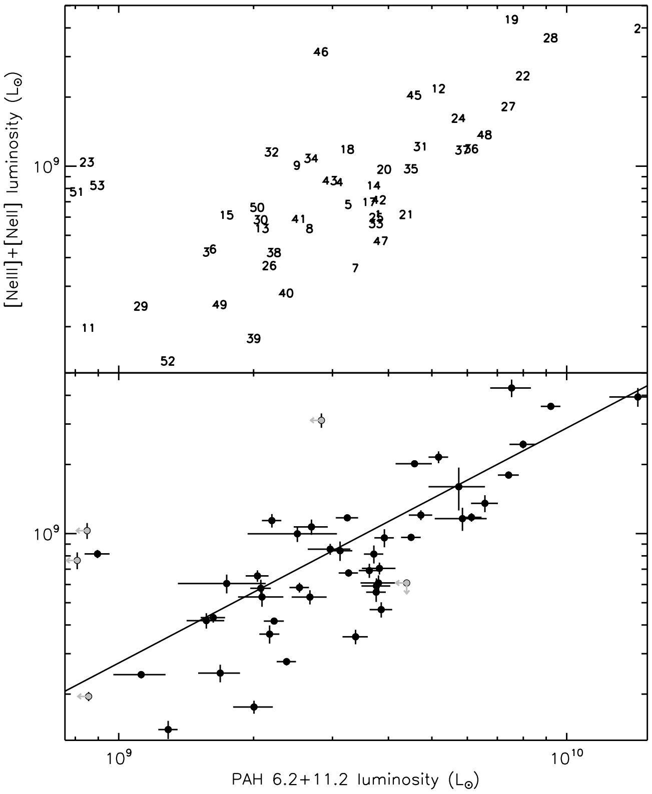

FIG. 15.—Total luminosity of the [Ne III] λ15.55 and [Ne II] λ12.81 lines vs. the total luminosity of the PAH 6.2 and 11.2 μm features. ULIRGs with detections on both axes are plotted in black, while ULIRGs with limits on one or both axes are plotted in gray. The solid line indicates the best fit to the data, given in eq. (3).

the 11.2 μm feature can be significantly affected by silicate absorption at 9.7 μm, we use the luminosities of the PAH 6.2 and 11.2 μm features. These PAH luminosities are measured from the low-resolution IRS spectra presented in V. Desai et al. (2007, in preparation). For the 11.2 μm PAH feature the luminosity was measured by integrating over 10.8–11.8 μm in the continuum-subtracted spectra, with the equivalent width evaluated at 11.25 μm. The relevant parameters for the 6.2 μm PAH feature were 5.90–6.55 and 6.22 μm, respectively.

In Figure 15 we plot [Ne III] + [Ne II] luminosity against the combined luminosities of the PAH 6.2 and 11.2 μm features.[10] The neon line luminosities and PAH luminosities clearly track each other, lending support to the idea that, on average, lower ionization neon lines originate in regions heated mostly by star formation. A power-law fit yields

$$L_N = (0.17^{+0.46}_{-0.12}) \times L_P^{1.02\pm0.05}, \qquad (3)$$

where L_N and L_P are the [Ne III] + [Ne II] and 6.2 + 11.2 μm luminosities (in any units, as long as they are both the same), respectively. Equation (3) is solely intended to indicate the trend, and evidently is not a good physical model for the data. It is notable, however, that the scaling between [Ne III] + [Ne II] luminosity and PAH 6.2 + 11.2 μm luminosity predicted from this fit is, to within the error on the exponent of L_P, linear. Interestingly, we see a comparable slope (although different normalization) if we instead plot [S III] λ18.713 luminosity against PAH 6.2 + 11.2 μm luminosity. This is consistent with the idea that the sizes of the lower ionization neon and sulfur emiting regions, and PAH-emitting regions in ULIRGs scale linearly with each other with increasing luminosity, although a luminosity dependence on metallicity and/or electron density could also play a role.

It is also straightforward to derive a relation between PAH 6.2 + 11.2 μm luminosity and star formation rate, using equation (12) from Ho & Keto (2007) combined with equation (3). In doing so, however, we use the updated conversion between Lyman continuum flux and star formation rate given by Hirashita et al. (2003) rather than the relation in Kennicutt (1998). By combining equation (12) from Ho & Keto (2007) with the relations between Lyman continuum flux and star formation rate given in § 2.1 of Hirashita et al. (2003) we obtain

$$\mathrm{SFR}(M_\odot\ \mathrm{yr}^{-1}) = 2.69 \times 10^{-41} \frac{L_N(\mathrm{ergs\ s}^{-1})}{f_{\mathrm{ion}}(f_{\mathrm{Ne}^+} + 1.67 f_{\mathrm{Ne}^{++}})}, \qquad (4)$$

where SFR is the star formation rate, L_{neon} is the combined luminosity of the two neon lines, f_{ion} is the fraction of photons that actually contribute to ionizing the gas, and f_{Ne^+} and $f_{\mathrm{Ne}^{++}}$ are the fractional abundances of [Ne II] and [Ne III], respectively. For ULIRGs, however, there is an additional complication. The conversion in Hirashita et al. (2003) assumes continuous star formation over $\gtrsim 10^8$ years. Star formation in ULIRGs, however, is likely to occur in some form of "burst" over timescales of 10^7–10^8 yr. This means that the star formation rates in ULIRGs will be underestimated by a significant amount if the conversion in equation (4) is used unmodified. Following previous work (Kennicutt 1998; Thornley et al. 2000), we adopt an *approximate* upward scaling of 50% to correct for this difference. This scaling is likely to be sufficient for considering trends, but should be adjusted for specific objects where the age and nature of the burst are known. Assuming this scaling, plus linear scaling between neon and PAH luminosity, $f_{\mathrm{ion}} = 0.6$, $f_{\mathrm{Ne}^+} = 0.75$ and $f_{\mathrm{Ne}^{++}} = 0.1$ (Ho & Keto 2007), we arrive at

$$\mathrm{SFR}(M_\odot\ \mathrm{yr}^{-1}) = 1.18 \times 10^{-41} L_P(\mathrm{ergs\ s}^{-1}), \qquad (5)$$

where L_P is in units of ergs s^{-1}. This assumes solar metallicity and a Salpeter IMF spanning 0.1–100 $M_\odot$, and is only applicable to objects where the PAH and neon luminosities arise from recent star formation.

The errors on the star formation rates derived using equation (5) are difficult to quantify. The conversion from Lyα continuum flux to star formation rate has an error of $\sim$30% (Kennicutt 1998), and there is a significant extra error introduced by the scatter in Figure 15. We therefore estimate that the errors on star formation rates derived using equation (5) are of order 30% for population studies, rising to at least 50% for individual objects. Equation (5) does, however, offer the advantage that it does not require an accurate measure of the rest-frame 1–1000 μm luminosity, and hence is particularly suited to population studies at high redshifts. Equation (5) also gives plausible star formation rates for our sample. We defer a complete analysis to an upcoming paper, but note that for Arp 220 and using the PAH luminosities in V. Desai et al. (2007, in preparation) equation (5) gives a star formation rate of 57 $M_\odot$ yr^{-1}, which is consistent with the total star formation rate inferred from radio observations, which give 50–100 $M_\odot$ yr^{-1} (Smith et al. 1998, but see also Parra et al. 2007).

4.2.3. *Starburst versus AGN Diagnostics*

To distinguish between starburst and AGN power behind the 1–1000 μm emission in ULIRGs, we need diagnostics that are sensitive to the observable differences between young stars and

---

[10] A similar plot but using only the 6.2 μm luminosity or the 11.2 μm luminosity yield plots with significantly greater scatter.

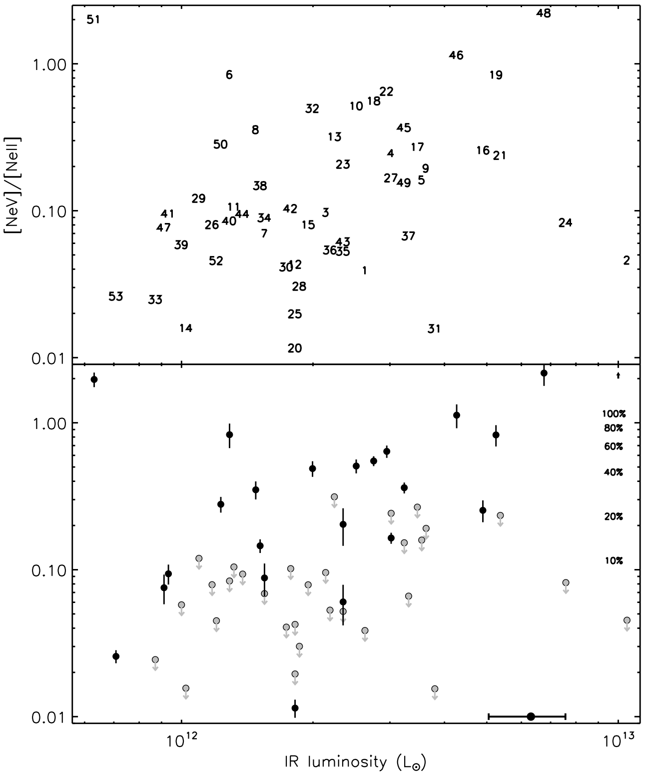

FIG. 16.—[Ne V] $\lambda 14.32$/[Ne II]$\lambda 12.81$ vs. infrared luminosity. The percentages on the y-axis indicate the predicted AGN contribution to the IR luminosity (Sturm et al. 2002). ULIRGs with detections on both axes are plotted in black, while ULIRGs with limits on one or both axes are plotted in gray. The small arrow indicates the effect on a points position if the V-band extinction toward the line-emitting regions is increased by $A_V = 30$. The horizontal bar on the bottom left indicates a 20% error on the IR luminosity.

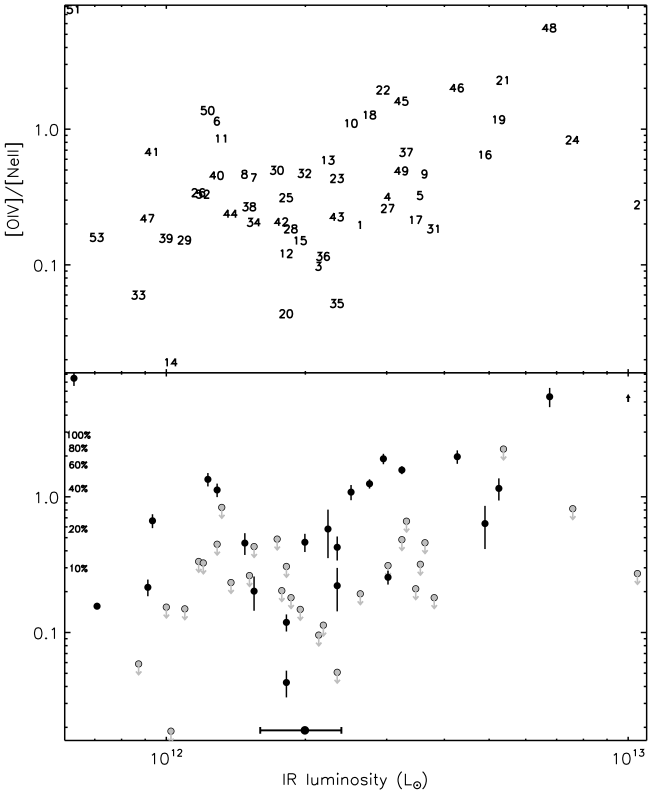

FIG. 17.—[O IV] $\lambda 25.89$/[Ne II] $\lambda 12.81$ vs. infrared luminosity. Other data and symbols are the same as in Fig. 16.

an accretion disk around a supermassive black hole. For our purposes, there are two such differences. First, the ionizing radiation from an AGN is harder and (potentially) more intense than that from a starburst. Second, AGNs occupy a smaller volume, ~0.1 pc, as opposed to a few tens to a few hundreds of pc for a starburst. In principle therefore, we might expect the averaged mid-IR spectra of AGNs to exhibit three differences compared to those of starbursts: higher ionization fine-structure lines, increased quantities of "hot" ($\gtrsim 100$ K) dust, and (potentially) increased obscuration. We explore each of these differences in this section.

We start with the simplest possible diagnostic; the detection (or otherwise) of individual lines. For examining starburst and AGN activity, the [Ne V] $\lambda 14.32$ and [O IV] $\lambda 25.89$ lines are the most useful single line diagnostics. Both lines can be strong in planetary nebulae and young supernova remnants (Oliva et al. 1999), and [O IV] is sometimes seen in Wolf-Rayet star spectra. Both lines are, however, weak in spectra of star-forming regions (e.g., Lutz et al. 1998), while being strong in spectra of AGNs. As [Ne V] $\lambda 14.32$ has $E_{\rm ion} = 97.1$ eV, compared to 54.9 eV for [O IV] $\lambda 25.89$, and because models indicate that [Ne V] $\lambda 14.32$ is unlikely to be strong in galaxies without an AGN (Voit 1992), we focus most of our attention on the [Ne V] $\lambda 14.32$ line.

The presence of [Ne V] $\lambda 14.32$ cannot provide meaningful constraints on the bolometric luminosity of an AGN, simply because a comparable [Ne V] $\lambda 14.32$ flux can be produced by a faint AGN with low obscuration, or a luminous AGN with high obscuration. From Table 3, however, we can see that [Ne V] $\lambda 14.32$ is detected in 22 out of 53 objects, providing direct spectroscopic evidence for an AGN in these 22 objects. Our sample is flux- rather than volume-limited, hence we cannot draw firm conclusions about local ULIRGs as a whole; however, this suggests that an AGN provides a nonnegligible fraction of the mid-IR flux in ~42% of local ULIRGs. This is significantly higher than the fraction of ULIRGs that show spectroscopic signatures of AGN activity in their optical or near-IR spectra, 20%–25% (Veilleux et al. 1999), although strictly speaking the Veilleux et al. 1999 sample and our sample are not directly comparable as their selections are different. Interestingly, we see no convincing trend in the detection of [Ne V] $\lambda 14.32$ as a function of IR luminosity. From Table 3 the ULIRGs with a [Ne V] $\lambda 14.32$ detection are fairly evenly spread between IR luminosities of $10^{11.80}$ $L_\odot$ and $10^{12.88}$ $L_\odot$; 10/22 ULIRGs with a [Ne V] $\lambda 14.32$ detection have $L_{\rm IR} > 10^{12.38}$ $L_\odot$, while 20/53 of the whole sample have $L_{\rm IR} > 10^{12.38}$ $L_\odot$. This contrasts with optical/near-IR spectroscopic surveys, which report a rising fraction of ULIRGs with AGN signatures, reaching 35%–50% at $>10^{12.38}$ $L_\odot$ (Veilleux et al. 1999).[11] A plausible reason for this discrepancy is high levels of extinction toward the nuclei of ULIRGs. From § 4.2.1, the increase in extinction toward the nuclei of ULIRGs compared to lower luminosity systems is of the order $A_V \simeq 40$, making it harder to see AGN signatures in the optical or near-IR. Mid-infrared spectroscopy, on the other hand, appears to be a sensitive probe of the presence or otherwise of AGNs in IR-luminous systems. We detect [O IV] $\lambda 25.89$ in 21/22 objects that show [Ne V] $\lambda 14.32$, and detect [O IV] $\lambda 25.89$ in only two objects that do not show [Ne V] $\lambda 14.32$, suggesting that [O IV] $\lambda 25.89$ is a good, but not perfect proxy for [Ne V] $\lambda 14.32$.

We next consider diagnostics based on fine-structure line ratios. In Figures 16 and 17 we plot [Ne V]/[Ne II] and [O IV]/[Ne II]

---

[11] The "boundary" luminosity quoted by Veilleux et al. 1999 is $10^{12.30} L_\odot$; however, this is for $H_0 = 75$ km s^{-1} Mpc^{-1} and $q_0 = 0.0$.

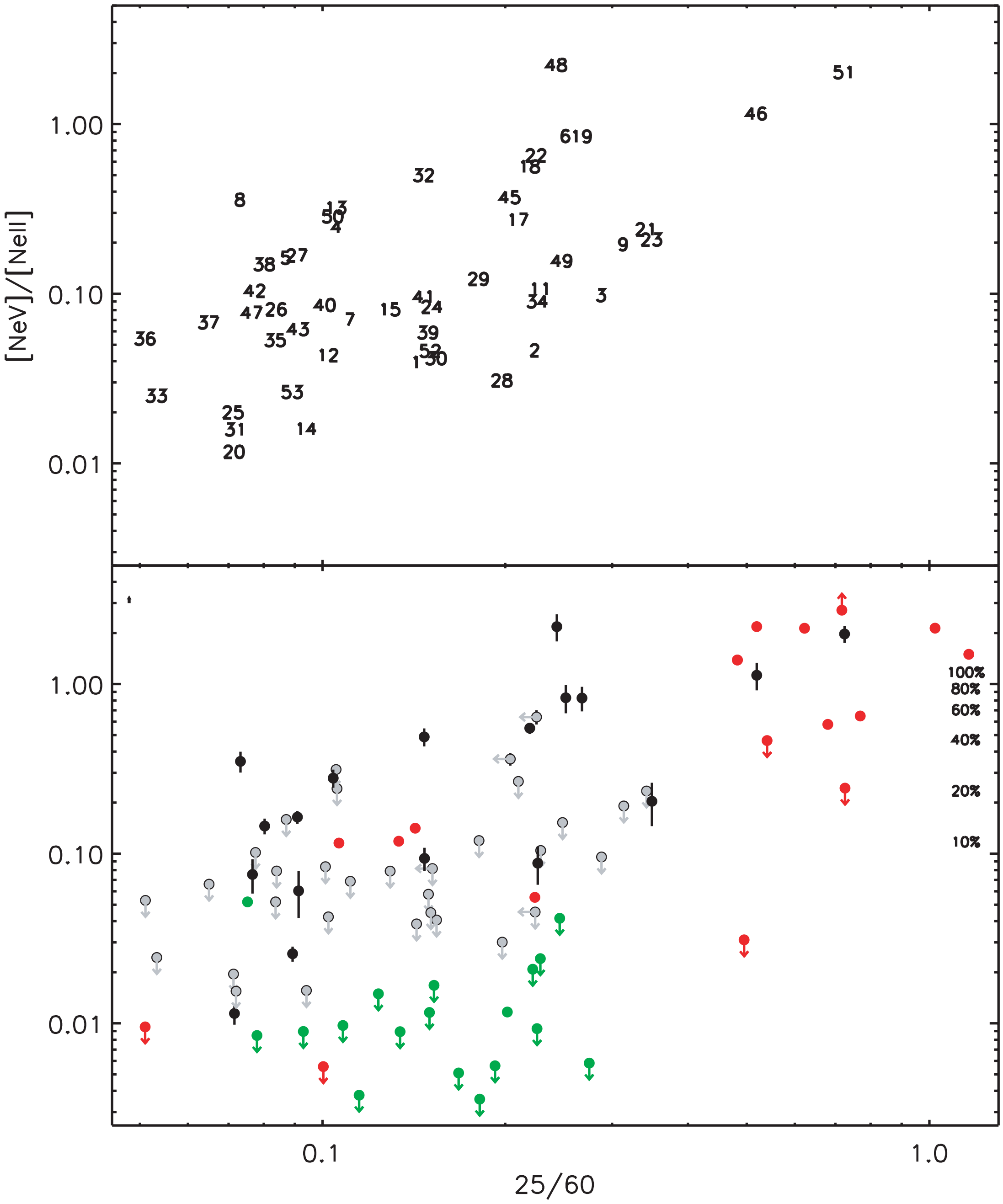

FIG. 18.—[Ne v] λ25.89/[Ne II] λ12.81 vs. *IRAS* 25/60 color. The green and red points are comparison starbursts and AGNs, respectively, but unlike Fig. 11, these samples are taken from Brandl et al. (2006) and Weedman et al. (2005), respectively. Other data and symbols are the same as in Fig. 16.

against IR luminosity, together with the predicted AGN contribution to the total IR luminosity based on these line ratios (Sturm et al. 2002). Both diagrams predict a broad spread in power source, ranging from 100% starburst to 100% AGN. In both diagrams, however, only 10-12 ULIRGs are above the 40% AGN line, and more than half the sample lie below the 20% lines. This is consistent with star formation being the dominant contributor to the IR emission in most ULIRGs, with only 20% of ULIRGs hosting an AGN with a comparable or greater IR luminosity than the starburst, in agreement with studies at other wavelengths (Veilleux et al. 1999; Farrah et al. 2003; Franceschini et al. 2003). There are, however, many caveats in using such simple diagnostics (Sturm et al. 2002), and Figures 16 and 17 should not be considered reliable diagnostics of the power source in individual ULIRGs, but rather as crude indicators of trends. It is, however, notable that we seem to have results consistent with other diagnostics for (some) individual objects. For example, both diagrams predict a small contribution from an AGN in Arp 220, consistent with results from the X-ray (Clements et al. 2002) and from *ISO* (Sturm et al. 1996), and 3C 273, Mrk 1014, Mrk 463E, and IRAS 05189−2524 are all predicted to contain a luminous AGN, in line with previous work (Shakura & Sunyaev 1976; Mazzarella et al. 1991; Boller et al. 2002; Farrah et al. 2005).

Given the likely origin of the [Ne v] λ14.32 line in AGNs, we can use the [Ne v]/[Ne II] ratio to test other mid-IR AGN diagnostics. One such diagnostic is the *IRAS* 25/60 μm flux density ratio; it has been suggested that "warm" objects (those with $f_{25}/f_{60} > 0.2$) are more likely to contain an AGN than "cool" ($f_{25}/f_{60} < 0.2$) objects (de Grijp et al. 1985; Sanders et al. 1988). In Figure 18 we plot [Ne v]/[Ne II] against f_{25}/f_{60}. Just over half

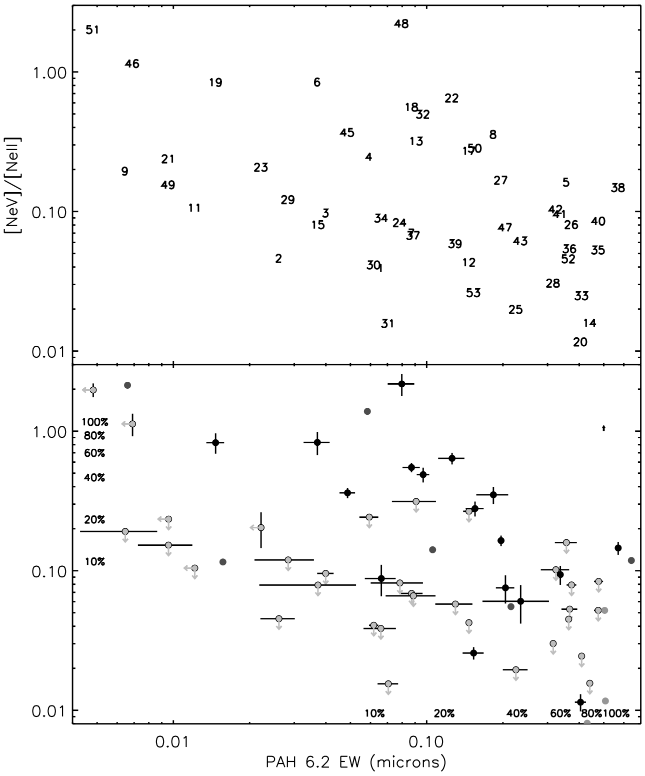

Fig. 19.—[Ne v] λ14.32/[Ne ii] λ12.81 vs. the equivalent width of the PAH 6.2 μm feature. The percentages on the *x*-axes indicate the predicted contribution to the IR luminosity from an starburst (Armus et al. 2007). Other data and symbols are the same as in Fig. 16. [*See the electronic edition of the Journal for a color version of this figure.*]

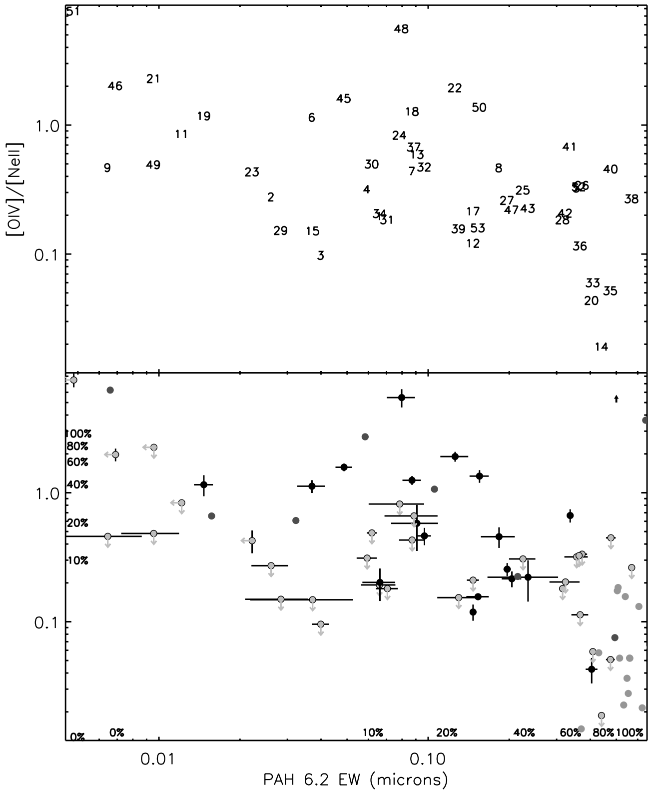

Fig. 20.—[O iv] λ25.89/[Ne ii] λ12.81 vs. the equivalent width of the PAH 6.2 μm feature. Other data and symbols are the same as in Fig. 19. [*See the electronic edition of the Journal for a color version of this figure.*]

of the "warm" objects have [Ne v] λ14.32 detections, compared to about one-third of the "cool" objects. Furthermore, for those objects with [Ne v] λ14.32 detections, the "warm" objects have systematically higher [Ne v]/[Ne ii] ratios than the cool objects. While our small sample sizes (particularly for the warm objects) render any conclusions tentative, we infer from this that the IRAS 25/60 μm flux density ratio is a reasonably good, although not perfect diagnostic for the presence of an IR-luminous AGN in a ULIRG.

We move on to consider diagrams with a diagnostic of the starburst and AGN luminosities on both the *x* and *y* axes. A natural diagnostic to combine with a fine-structure line ratio is a measure of the strength of the PAH features. To measure PAH strength we use the equivalent width (EW) of the 6.2 μm PAH feature, taken from V. Desai et al. (2007, in preparation) as this feature is strong, and lies in a relatively uncluttered part of the mid-IR spectra of ULIRGs, although its use does depend on an accurate correction for water ice and/or aliphatic hydrocarbon absorption. A mid-IR fine-structure line ratio versus PAH EW diagnostic diagram has been used by several authors for many classes of IR-luminous galaxy (e.g., Genzel et al. 1998; Sturm et al. 2002).

In Figures 19 and 20 we plot [Ne v]/[Ne ii] and [O iv]/[Ne ii] against the equivalent width of the 6.2 μm PAH feature, together with the linear mixing ratios from Sturm et al. (2002) and Armus et al. (2007). Here we again see a broad spread in fractional AGN and starburst luminosities, from "pure" AGNs to "pure" starbursts. Those sources classified by Figures 19 and 20 as AGN-dominated tend to have $\mathrm{PAH}_{\mathrm{EW}}^{6.2\,\mu\mathrm{m}} \lesssim 0.05$, [Ne v]/[Ne ii] $\gtrsim 0.2$, and [O iv]/[Ne ii] $\gtrsim 0.5$, whereas the "pure" starbursts tend to have $\mathrm{PAH}_{\mathrm{EW}}^{6.2\,\mu\mathrm{m}} \gtrsim 0.2$, [Ne v]/[Ne ii] $\lesssim 0.09$, and [O iv]/[Ne ii] $\lesssim 0.2$. The IR emission from the majority of the sample are still predicted to be powered mainly by star formation, although this trend is not so clear as from Figure 16. We see broad (to within a factor of 3) agreement between the two axes, and also that no object lies in the "forbidden" top right-hand corner of either diagram. In both diagrams, the six objects which show a detection of the [Cl ii] λ14.37 line (§ 3.2) are mostly located toward the right-hand side, consistent with the postulated origin of this line in star-forming regions.

It is, however, notable that several sources lie in a "forbidden" region in each diagram, where the PAH equivalent widths suggest a low starburst contribution, but the fine-structure line ratios suggest a low AGN contribution. There are, broadly, four possible reasons for this discrepancy:[12] (1) underestimated 6.2 μm PAH EWs due to nearby water ice and/or aliphatic hydrocarbon absorption, (2) destruction of PAHs in *luminous* starburst environments (Rigopoulou et al. 1999; Farrah et al. 2003; Beirão et al. 2006), (3) suppression of PAH EWs in *compact* starburst environments, and (4) increased general obscuration levels. We do not consider the first two possibilities likely though. We have in all cases used ice absorption-corrected values for the 6.2 μm PAH EWs (the correction is of order 10% for the 6.2 μm feature and less than 5% for the 11.2 μm feature; Spoon et al. 2007, in preparation) and it is unlikely that any residual ice absorption could shift sources by such a significant distance on this plot. If the PAHs were being destroyed in extremely luminous starbursts then we would expect the objects in the "forbidden" region to all have high-IR luminosities, but the objects in this region (e.g., IRAS

---

[12] A fifth possibility is variation in the filling factor of the coronal-line region clouds. A low filling factor would imply a small ionization parameter *U*, and would therefore give an unusually low [Ne v]/[Ne ii] ratio, for example. We do not, however, have the data to address this possibility.

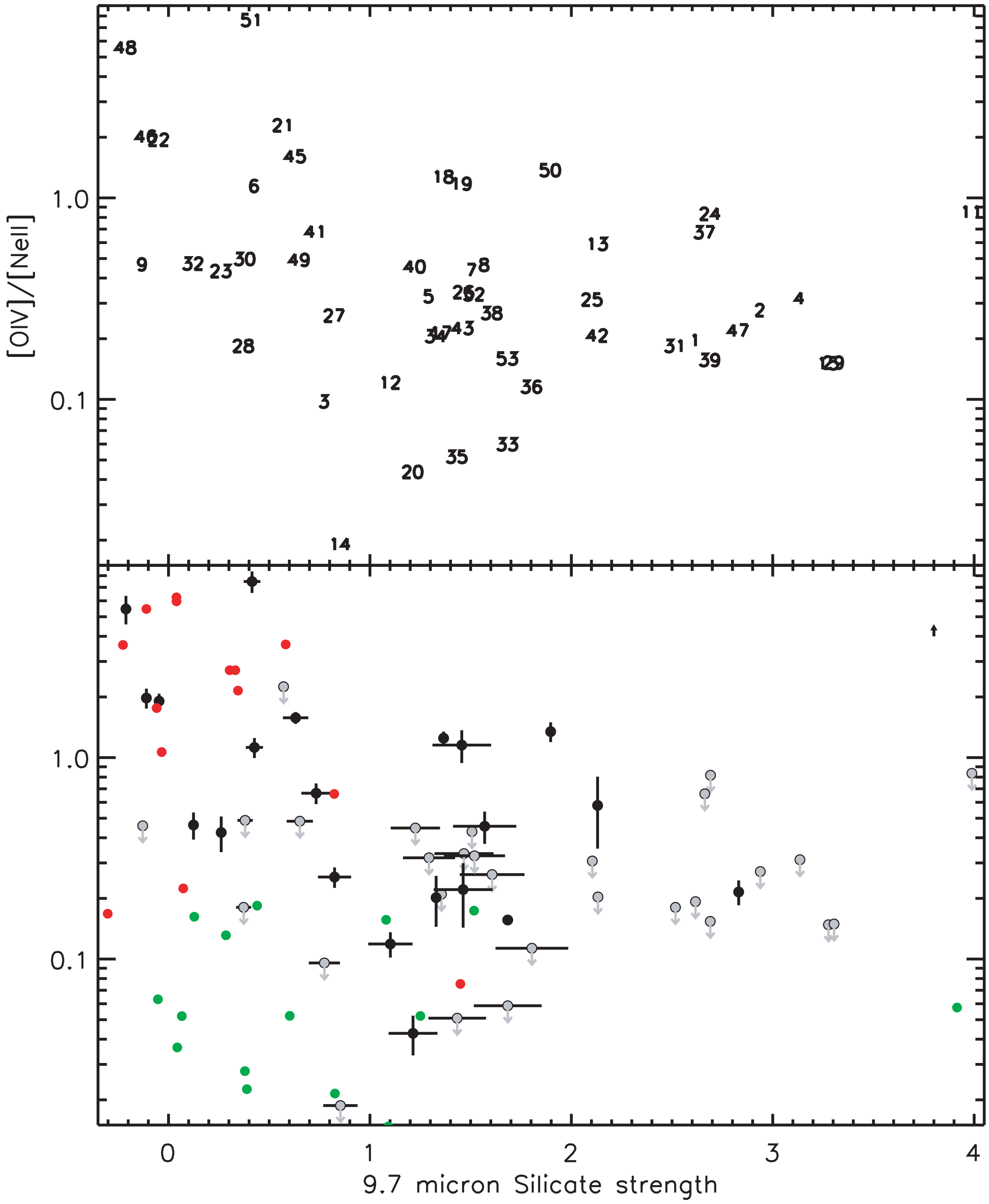

Fig. 21.—[O IV] $\lambda25.89$/[Ne II] $\lambda12.81$ vs. the strength of the 9.7 μm silicate feature. Other data and symbols are the same as in Fig. 19.

08572+3915, IRAS 00397−1312, IRAS 15462−0450) span a wide range in IR luminosity. A combination of increased overall obscuration and increased starburst compactness therefore seem the most likely culprits. The mixing ratios in both diagrams are based on starbursts and AGNs with IR luminosities of 10^{10}–10^{11} $L_{\odot}$. Their use therefore assumes a linear scaling between starburst and AGN luminosity, and overall obscuration and starburst geometry, to give rise to comparable observed [Ne V]/[Ne II] and [O IV]/[Ne II] ratios and PAH 6.2 μm EWs. These assumptions are unlikely to be valid. For example, previous authors have noted A_{λ} values of 10 or more, even in the mid-IR (Genzel et al. 1998), and we derived $A_V \simeq 40$ over and above lower luminosity starbursts in § 4.2.1. Increased overall obscuration will lead to greater suppression of the [Ne V] and [O IV] lines compared to the [Ne II] line, as these regions must lie closer to the starburst and/or AGN. This increased obscuration will also arise in lower than expected PAH luminosities, but is unlikely to affect their EWs. However, we expect more compact starbursts to have a stronger mid-IR continuum, which will lead to suppression of PAH EWs. Therefore, increased overall obscuration combined with more spatially compact starbursts in ULIRGs compared to lower luminosity systems can plausibly explain the outliers in Figures 19 and 20.

An important caveat, however, is that diagrams like Figures 19 and 20 are not suited to studying the physics of individual objects, and can often get the answers wrong. For example, if the power source is so obscured that it does not emit significantly at wavelengths shortward of ~25 μm, then mid-IR fine-structure line ratio versus PAH EW diagnostic plots can give misleading results (Peeters et al. 2004). Some "outliers" are therefore understandable. One example is IRAS 15206+3342 (No. 28). This object lies

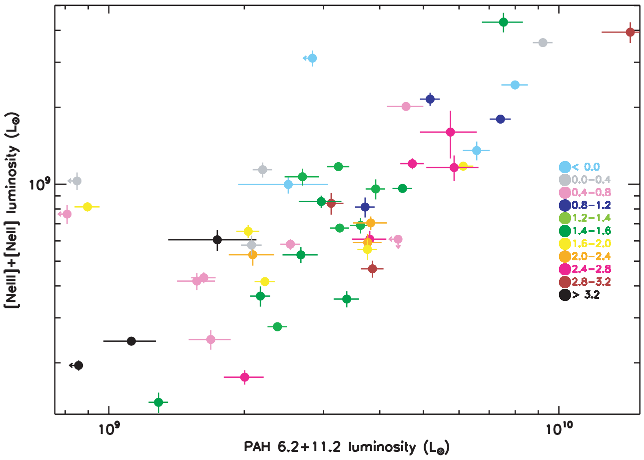

FIG. 22.—Total luminosity of the [Ne III] $\lambda15.55$ and [Ne II] $\lambda12.81$ lines vs. the total luminosity of the PAH 6.2 and 11.2 μm features. The points are color coded according to the strength of the 9.7 μm silicate feature.

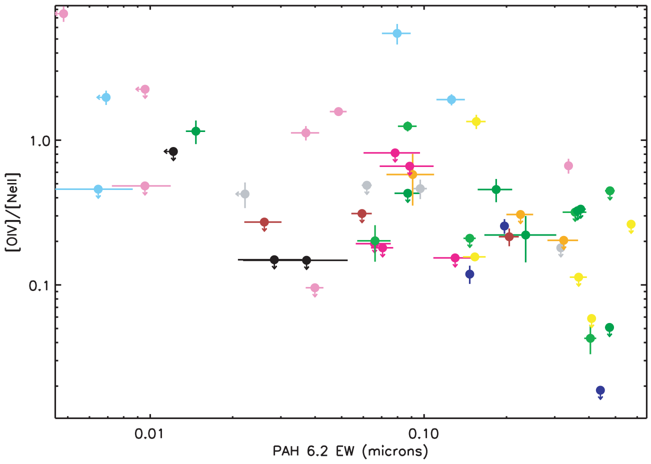

FIG. 23.—[O IV] $\lambda25.89$/[Ne II] $\lambda12.81$ vs. the equivalent width of the PAH 6.2 μm feature, with the points coded according to the strength of the 9.7 μm silicate feature. The color coding is the same as in Fig. 22. Here we see that the lightly obscured and heavily obscured systems lie mostly on the left-hand side of the plot, whereas moderately obscured systems lie mainly toward the right-hand side of the plot.

squarely in the "starburst" part of both plots, and from this one might conclude that it does not contain an energetically significant AGN. Its UV spectrum (Farrah et al. 2005), however, shows clear evidence for a broad absorption line QSO. A second example is NGC 6240, which also lies in the "starburst" part of both plots, despite the extensive evidence for an IR-luminous AGNs in this source (Armus et al. 2006). The key point is that diagnostics such as those in Figures 19 and 20 probe the physics of specific environments within ULIRGs. To obtain a complete picture of an individual object therefore requires multiple diagnostics to probe multiple environments.

4.2.4. *Silicate Absorption*

We explore the issue of mid-IR obscuration in ULIRGs further by combining the diagnostics discussed previously with a measure of the strength of the 9.7 μm silicate absorption feature, $S_{\rm sil}$:

$$S_{\rm sil} = \ln\left(\frac{F_{\rm obs}(9.7\ \mu{\rm m})}{F_{\rm cont}(9.7\ \mu{\rm m})}\right), \qquad (6)$$

where $F_{\rm obs}$ is the observed flux at rest-frame 9.7 μm, and $F_{\rm cont}$ is the underlying continuum flux at rest-frame 9.7 μm deduced from a spline fit to the continuum flux at rest frame 5.0–7.0, 14.0–14.5, and 25.0–40.0 μm. A complete description of the method used to measure $S_{\rm sil}$ can be found in Spoon et al. (2006) and Levenson et al. (2007). The silicate strengths for our sample are measured from the low-resolution spectra, and are presented in Spoon et al. (2007, in preparation).

In Figure 21 we plot $S_{\rm sil}$ against the [O IV]/[Ne II] line ratio, along with the "reference" starbursts and AGNs (Brandl et al. 2006; Weedman et al. 2005). The reference starbursts and AGNs separate well on the y-axis, with most of the AGNs above [O IV]/[Ne II] $= 0.2$ and most of the starbursts below. Nearly all the starbursts and AGNs are confined to $-0.5 < S_{\rm sil} < 2.0$. The ULIRGs are found over the whole range of [O IV]/[Ne II] ratios where the reference samples are seen, but are offset on the x-axis, with greater silicate strengths for a given [O IV]/[Ne II] ratio. The simplest interpretation of this is that the starbursts in ULIRGs are similar in nature to those in lower luminosity systems, but with significantly greater (A_V values of a few tens) total obscuration, consistent with the conclusion in § 4.2.1.

It would be natural, from this, to postulate that silicate strength is a measure of the total obscuration of the starburst. If so, then we might expect a correlation between star formation rate and silicate strength; the reasoning being that a more luminous starburst will have a deeper 9.7 μm absorption feature as the starburst has an increased total dust column. It is straightforward to test this hypothesis; in Figure 22 we duplicate Figure 15, but this time color-coded each object according to its silicate strength. Clearly, there is no correlation. Objects with the strongest silicate absorption seem to be confined to the lower left of the plot, although with only three objects it is impossible to draw firm conclusions. The other objects seem to be scattered randomly; strongly absorbed and weakly absorbed sources are found from the top right to the bottom left. Furthermore, if $S_{\rm sil}$ was simply a measure of the obscuration of the starburst, then we would expect the sources with the greatest negative offset from the Ho & Keto line in Figure 15 to have the largest values of $S_{\rm sil}$, but this is not the case. For example, three of the sources with the greatest negative offset in Figure 15, IRAS 06035−7102, IRAS 20551−4250, and 3C 273, range from having a deep silicate absorption feature to a silicate emission feature. We infer from this that silicate strength is not simply a measure of the total obscuration of the starbursts in ULIRGs. A similar conclusion was reached by Higdon et al. (2006) based on the molecular hydrogen line strengths.

We move on to consider a different scenario, in which the 9.7 μm silicate absorption in ULIRGs is affected by the AGN as well as, or instead of, the starburst. To examine this possibility we duplicate the plot in Figure 20 in Figure 23, again color-coding each point by its silicate strength. From this we see that both strongly and weakly absorbed sources are found across the span of the plot, and there is no appreciable trend in *average* silicate strength in any direction. There is, however, one interesting trend. Those sources toward the left-hand side of the diagram tend to have either very deep absorption, or very shallow to no absorption, whereas those objects on the right-hand side of the plot seem to be almost universally "averagely" absorbed. Of the 13 objects on the right-hand side, all but two (IRAS 15206+3342 and IRAS 23128−5919) have $0.8 < S_{\rm sil} < 2.4$. Of the 13 objects on the left-hand side, only one (IRAS 12514+1027) does not satisfy $S_{\rm sil} > 2.4$ or $S_{\rm sil} < 0.8$. Overall, there is a clear shift in the distribution of values of $S_{\rm sil}$ as we move from the left-hand side to the right-hand side of the plot, from a single, broad peak centered at around $S_{\rm sil} \simeq 1.5$ to two narrower peaks, one at $S_{\rm sil} \simeq 2.8$ and one at $S_{\rm sil} \simeq 0.2$. This shift is conceptually similar to the "fork" diagram in Spoon et al. (2006).

These distributions in silicate strength can be interpreted in one of two ways. The first is that very strong or very weak silicate absorption indicates the presence of an AGN, with moderate silicate absorption indicating the presence of a starburst. For an AGN, we expect a strong dependence of observed properties on viewing angle, as nearly all lines of evidence suggest that the dust in AGNs is arranged in a planar structure, whether that structure is a torus (Schartmann et al. 2005), a flared disk (Fritz et al. 2006), or discrete clouds (Elitzur & Shlosman 2006). For a starburst, however, we expect a weaker (although still possibly significant) dependence on viewing angle; millimeter interferometry has shown that the starburst regions in ULIRGs are dense and compact (Tacconi et al. 2006), while recent theoretical (e.g., Silk 2005) and indirect observational evidence suggests that starbursts in ULIRGs are unlikely to have a disklike structure (Fisher 2006). We therefore expect that the distribution of values of $S_{\rm sil}$ in obscured AGNs will be bimodal, with a high apparent obscuration when the AGN is viewed edge on, but low obscuration when the AGN is viewed face on, but that the dependence of $S_{\rm sil}$ on the viewing angle of the starburst will be weaker. This is supported by the fact that optical QSOs usually show silicates in emission (Hao et al. 2007), and that one of the two objects on the right-hand side of the lower panel of Figure 22 is IRAS 15206+3342, which, as previously mentioned, contains a BAL QSO.

The second way is that the sources with $S_{\rm sil} \gtrsim 2.4$ instead contain an extremely obscured starburst, and that only those sources with either a [Ne V] detection or a silicate feature in emission contain an IR-luminous AGN. This scenario is plausible as a very compact, highly obscured starburst could also result in suppression of PAH features, and would also explain the absence of [Ne V] detections (if the starburst surrounds the AGN) in the few objects on the left-hand side of Figure 23 with $S_{\rm sil} \gtrsim 2.4$. With the data available to us it is difficult to choose between these two possibilities. Both scenarios are consistent with the "fork" diagram in Spoon et al. (2006), for example. With some reserve therefore, we propose that the first scenario is more likely, and that moderate silicate absorption signifies the presence of a dominant starburst, but that very deep or very shallow silicate absorption in ULIRGs likely signifies the presence of a bolometrically significant AGN.

5. CONCLUSIONS

We have presented an atlas of fine-structure lines and other emission features measured from high-resolution mid-infrared spectra of 53 ULIRGs at $0.018 < z < 0.319$, taken using the Infrared Spectrograph onboard the *Spitzer Space Telescope*. We have employed a variety of diagnostics using these emission lines as well as those based on PAH features and the strength of the 9.7 μm silicate absorption feature to investigate the power source behind the infrared emission. Our conclusions are the following:

1. All of the spectra show various of fine-structure emission lines of neon, oxygen, and sulfur, as well as one or more molecular hydrogen lines. We see the [Ne II] λ12.81, [Ne III] λ15.56, and [S III] λ18.71 in most of the sample, and [S IV] λ10.51 in just under half the sample. The higher ionization lines [Ne V] λ14.32 and [O IV] λ25.89 are detected in just under half the sample, while [Ne V] λ24.32 is detected in about one-third of the sample. Rarer lines include [Cl II] λ14.37 (six objects), H I 7–6 λ12.37 (four objects), [P III] λ17.89 (two objects), and [Ar V] λ13.10 (two objects). Some objects also show low-ionization iron lines, including [Fe II] $\lambda\lambda$17.94, 24.52, 25.99 and [Fe III] λ22.93. The detection of three further lines is dependent on redshift, but we see [S III] λ33.48 in ~80% of the objects where this line lies within the bandpass, [Ar II] λ8.99 in just over 50%, and [S III] λ34.82 in just over 50%.

2. The presence of the [Ne V] λ14.32 μm line in 22/53 objects is direct spectroscopic evidence for the presence of an AGN that provides a significant, although not necessarily dominant, fraction of the mid-IR flux in ~42% of ULIRGs. Based on this, we find that the IRAS 25/60 μm flux density ratio is a reasonable, although not perfect, diagnostic for the presence of an IR-luminous AGN in ULIRGs. In most, but not all objects where we see [Ne V] λ14.32 μm we also see [O IV] λ25.89, suggesting that [O IV] λ25.89 is a good proxy for the [Ne V] λ14.32 μm. In contrast, we see [S IV] λ10.51 in a surprisingly low fraction of the sample, given that its ionization energy is comparable to that of [Ne III] λ15.56, and that the H_2, $S(3)$ λ9.66 line is seen in most of our sample. The most likely reason for this is that the neon- and sulfur-emitting zones in our samples lie within regions that are more strongly extincted by silicate dust than the H_2-emitting regions; the increased extinction due to the nearby 9.7 μm absorption feature would then weaken the apparent flux of [S IV] λ10.51 relative to [Ne III] λ15.56.

3. We use the [Ne III]/[Ne II] versus [S IV]/[S III] plane to show that the excitation levels in the mid-IR-emitting regions span more than 2 orders of magnitude in both the neon and sulfur line ratios. The range in both line ratios is comparable to that seen in starbursts and AGNs with IR luminosities in the range $10^{10} < L_{\rm IR}(L_\odot) < 10^{11.5}$, but we see a systematically lower [Ne III]/[Ne II] ratio for a given [S IV]/[S III] in our sample compared to systems with IR luminosities of $<10^{10}\ L_\odot$, possibly due to the increased density of gas in the NLR of ULIRGs. We use the [Ne V] 14.32 μm/[Ne V] 24.32 μm and the [S III]1 8.71 μm/[S III] 33.48 μm line ratios to show that the electron densities in the mid-IR-emitting regions of ULIRGs are $<10^4$ cm^{-3} in all cases, well below the critical densities.

4. We show that the combined luminosity of the [Ne III] λ15.56 and [Ne II] λ12.81 lines correlates with both total IR luminosity (Fig. 14), and the combined luminosity of the PAH 6.2 and 11.2 μm features (Fig. 15). Combining this result with previous work (Ho & Keto 2007), we derive a calibration between star formation rate and PAH 6.2 + 11.2 μm luminosity for ULIRGs:

$$\mathrm{SFR}(M_\odot\ \mathrm{yr}^{-1}) = 1.18 \times 10^{-41} L_P(\mathrm{ergs\ s}^{-1}), \qquad (7)$$

where $\dot{M}_\odot$ is the star formation rate in solar masses per year, and L_P is the PAH 6.2 + 11.2 μm luminosity in ergs s^{-1}

5. We employ a variety of spectral diagnostics to show that, despite the presence of a luminous AGN in ~42% of ULIRGs, the most likely dominant contributor to the total IR emission in most ULIRGs is star formation, with an AGN providing a higher contribution than a starburst in only ~20% of ULIRGs. The fine-structure line ratios, luminosities and PAH EWs of our sample are consistent with the starbursts and AGNs in ULIRGs being more extincted ($A_V \simeq 40$), and for the starbursts more compact, versions of those in lower luminosity systems.

6. We show that the strength of the 9.7 μm silicate feature is unlikely to be a simple indicator of the total obscuration of the starburst. We combine measurements of PAH equivalent widths, 9.7 μm silicate feature strengths, and fine-structure line ratios to show that ULIRGs with silicate strengths of $S_{\rm sil} < 0.8$ likely contain an energetically significant AGN, whereas the IR emission from ULIRGs with $0.8 < S_{\rm sil} < 2.4$ is likely dominated by star formation. We postulate that ULIRGs with $S_{\rm sil} > 2.4$ contain an

deeply buried AGN, although a comparably obscured starburst is also possible.

We thank Xander Tielens and Javier Goicoechea for advice on OH$^-$ absorption features, and the referee for a very helpful report. This work is based on observations made with the *Spitzer Space Telescope*, which is operated by the Jet Propulsion Laboratory, California Institute of Technology under a contract with NASA. Support for this work was provided by NASA. This research has made extensive use of the NASA/IPAC Extragalactic Database (NED) which is operated by the Jet Propulsion Laboratory, California Institute of Technology, under contract with NASA.

REFERENCES

Alexander, D. M., Smail, I., Bauer, F. E., Chapman, S. C., Blain, A. W., Brandt, W. N., & Ivison, R. J. 2005, Nature, 434, 738

Alexander, T., Sturm, E., Lutz, D., Sternberg, A., Netzer, H., & Genzel, R. 1999, ApJ, 512, 204

Armus, L., et al. 2004, ApJS, 154, 178

———. 2006, ApJ, 640, 204

———. 2007, ApJ, 656, 148

Beirão, P., Brandl, B. R., Devost, D., Smith, J. D., Hao, L., & Houck, J. R. 2006, ApJ, 643, L1

Bernard-Salas, J., Peeters, E., Sloan, G. C., Cami, J., Guiles, S., & Houck, J. R. 2006, ApJ, 652, L29

Bernard-Salas, J., Pottasch, S. R., Beintema, D. A., & Wesselius, P. R. 2001, A&A, 367, 949

Blain, A. W., Chapman, S. C., Smail, I., & Ivison, R. 2004, ApJ, 611, 725

Boller, T., Gallo, L. C., Lutz, D., & Sturm, E. 2002, MNRAS, 336, 1143

Borys, C., Chapman, S., Halpern, M., & Scott, D. 2003, MNRAS, 344, 385

Brandl, B. R., et al. 2006, ApJ, 653, 1129

Bushouse, H. A., et al., 2002, ApJS, 138, 1

Chapman, S. C., Windhorst, R., Odewahn, S., Yan, H., & Conselice, C. 2003, ApJ, 599, 92

Chiar, J. E., & Tielens, A. G. G. M. 2006, ApJ, 637, 774

Clements, D. L., McDowell, J. C., Shaked, S., Baker, A. C., Borne, K., Colina, L., Lamb, S. A., & Mundell, C. 2002, ApJ, 581, 974

Cohen, M., Megeath, S. T., Hammersley, P. L., Martín-Luis, F., & Stauffer, J. 2003, AJ, 125, 2645

Condon, J. J., Cotton, W. D., Greisen, E. W., Yin, Q. F., Perley, R. A., Taylor, G. B., & Broderick, J. J. 1998, AJ, 115, 1693

Condon, J. J., Huang, Z.-P., Yin, Q. F., & Thuan, T. X. 1991, ApJ, 378, 65

Coppin, K., et al. 2006, MNRAS, 372, 1621

Dale, D. A., et al. 2006, ApJ, 646, 161

de Grijp, M. H. K., Miley, G. K., Lub, J., & de Jong, T. 1985, Nature, 314, 240

Dole, H., et al. 2001, A&A, 372, 364

Draine, B. T. 1989, in Proc. 22nd Eslab Symp., Infrared Spectroscopy in Astronomy, ed, B. H. Kaldeich (ESA SP-290; Noordwijk: ESA), 93

———. 2003, ARA&A, 41, 241

Dwek, E. 2005, in AIP Conf. Proc. 761, The Spectral Energy Distributions of Gas-Rich Galaxies: Confronting Models with Data, ed. C. C. Popescu & R. J. Tuffs (Melville: AIP), 103

Eales, S., Lilly, S., Webb, T., Dunne, L., Gear, W., Clements, D., & Yun, M. 2000, AJ, 120, 2244

Elitzur, M., Goldreich, P., & Scoville, N. 1976, ApJ, 205, 384

Elitzur, M., & Shlosman, I. 2006, ApJ, 648, L101

Farrah, D., Serjeant, S., Efstathiou, A., Rowan-Robinson, M., & Verma, A. 2002b, MNRAS, 335, 1163

Farrah, D., Surace, J. A., Veilleux, S., Sanders, D. B., & Vacca, W. D. 2005, ApJ, 626, 70

Farrah, D., Verma, A., Oliver, S., Rowan-Robinson, M., & McMahon, R. 2002a, MNRAS, 329, 605

Farrah, D., et al., 2001, MNRAS, 326, 1333

———. 2003, MNRAS, 343, 585

———. 2006a, ApJ, 641, L17

———. 2006b, ApJ, 643, L139

Fisher, D. B. 2006, ApJ, 642, L17

Fluks, M. A., Plez, B., The, P. S., de Winter, D., Westerlund, B. E., & Steenman, H. C. 1994, A&AS, 105, 311

Förster Schreiber, N. M., Roussel, H., Sauvage, M., & Charmandaris, V. 2004, A&A, 419, 501

Franceschini, A., et al., 2003, MNRAS, 343, 1181

Fritz, J., Franceschini, A., & Hatziminaoglou, E. 2006, MNRAS, 366, 767

Genzel, R., & Cesarsky, C. J. 2000, ARA&A, 38, 761

Genzel, R., et al., 1998, ApJ, 498, 579

Goicoechea, J. R., Martín-Pintado, J., & Cernicharo, J. 2005, ApJ, 619, 291

Hacking, P., Houck, J. R., & Condon, J. J. 1987, ApJ, 316, L15

Hao, L., Weedman, D. W., Spoon, H. W. W., Marshall, J. A., Levenson, N. A., Elitzur, M., & Houck, J. R. 2007, ApJ, 655, L77

Higdon, S. J. U., Armus, L., Higdon, J. L., Soifer, B. T., & Spoon, H. W. W. 2006, ApJ, 648, 323

Higdon, S. J. U., et al. 2004, PASP, 116, 975

Hirashita, H., Buat, V., & Inoue, A. K. 2003, A&A, 410, 83

Ho, L., & Keto, E. 2007, ApJ, in press (astro-ph/0611856)

Hony, S., Van Kerckhoven, C., Peeters, E., Tielens, A. G. G. M., Hudgins, D. M., & Allamandola, L. J. 2001, A&A, 370, 1030

Houck, J. R., Schneider, D. P., Danielson, G. E., Neugebauer, G., Soifer, B. T., Beichman, C. A., & Lonsdale, C. J. 1985, ApJ, 290, L5

Houck, J. R., et al. 2004, ApJS, 154, 18

Hughes, D. H., et al., 1998, Nature, 394, 241

Imanishi, M., Dudley, C. C., Maiolino, R., Maloney, P. R., Nakagawa, T., & Risaliti, G. 2007, ApJS, 171, 72

Joseph, R. D., & Wright, G. S. 1985, MNRAS, 214, 87

Justtanont, K., et al. 1996, A&A, 315, L217

Kawakatu, N., Anabuki, N., Nagao, T., Umemura, M., & Nakagawa, T. 2006, ApJ, 637, 104

Kennicutt, R. C., Jr. 1998, ARA&A, 36, 189

Kim, D.-C., & Sanders, D. B. 1998, ApJS, 119, 41

Klaas, U., et al. 2001, A&A, 379, 823

Kotak, R., et al. 2006, ApJ, 651, L117

Lahuis, F., et al. 2007, ApJ, 659, 296

Laurent, O., Mirabel, I. F., Charmandaris, V., Gallais, P., Madden, S. C., Sauvage, M., Vigroux, L., & Cesarsky, C. 2000, A&A, 359, 887

Lebofsky, M. J., & Rieke, G. H. 1979, ApJ, 229, 111

Levenson, N. A., Sirocky, M. M., Hao, L., Spoon, H. W. W., Marshall, J. A., Elitzur, M., & Houck, J. R. 2007, ApJ, 654, L45

Levine, D. A., et al. 1998, ApJ, 504, 64

Li, A., & Draine, B. T. 2001, ApJ, 554, 778

Lípari, S., Terlevich, R., Díaz, R. J., Taniguchi, Y., Zheng, W., Tsvetanov, Z., Carranza, G., & Dottori, H. 2003, MNRAS, 340, 289

Lonsdale, C. J., Diamond, P. J., & Smith, H. E. 1994, Nature, 370, 117

Lonsdale, C. J., Farrah, D., & Smith, H. E. 2006, in Astrophysics Update 2., ed. J. W. Mason (Heidelberg: Springer), 285

Lonsdale, C. J., Hacking, P. B., Conrow, T. P., & Rowan-Robinson, M. 1990, ApJ, 358, 60

Lonsdale C., J., Lonsdale Colin, J., Smith, H. E., & Diamond, P. J. 2003, ApJ, 592, 804

Lutz, D., Kunze, D., Spoon, H. W. W., & Thornley, M. D. 1998, A&A, 333, L75

Lutz, D., et al. 1996, A&A, 315, L137

Mazzarella, J. M., Soifer, B. T., Graham, J. R., Neugebauer, G., Matthews, K., & Gaume, R. A. 1991, AJ, 102, 1241

Nagar, N. M., Wilson, A. S., Falcke, H., Veilleux, S., & Maiolino, R. 2003, A&A, 409, 115

Oliva, E., Moorwood, A. F. M., Drapatz, S., Lutz, D., & Sturm, E. 1999, A&A, 343, 943

Parra, R., Conway, J. E., Diamond, P. J., Thrall, H., Lonsdale, C. J., Lonsdale, C. J., & Smith, H. E. 2007, 659, 314

Peeters, E., Spoon, H. W. W., & Tielens, A. G. G. M. 2004, ApJ, 613, 986

Peeters, E., et al. 2002, A&A, 381, 571

Ptak, A., Heckman, T., Levenson, N. A., Weaver, K., & Strickland, D. 2003, ApJ, 592, 782

Puget, J. L., & Leger, A. 1989, ARA&A, 27, 161

Puget, J.-L., et al. 1996, A&A, 308, L5

Reach, W. T., Morris, P., Boulanger, F., & Okumura, K. 2003, Icarus, 164, 384

Rieke, G. H., & Low, F. J. 1972, ApJ, 176, L95

Rigopoulou, D., Spoon, H. W. W., Genzel, R., Lutz, D., Moorwood, A. F. M., & Tran, Q. D. 1999, AJ, 118, 2625

Risaliti, G., Gilli, R., Maiolino, R., & Salvati, M. 2000, A&A, 357, 13

Rocca-Volmerange, B., Le Borgne, D., De Breuck, C., Fioc, M., & Moy, E. 2004, A&A, 415, 931

Roche, P. F., & Aitken, D. K. 1985, MNRAS, 215, 425

Roche, P. F., Aitken, D. K., & Smith, C. H. 1991, MNRAS, 252, 282

Rowan-Robinson, M., et al. 1997, MNRAS, 289, 490

Sanders, D. B., & Mirabel, I. F. 1996, ARA&A, 34, 749

Sanders, D. B., Soifer, B. T., Elias, J. H., Madore, B. F., Matthews, K., Neugebauer, G., & Scoville, N. Z. 1988, ApJ, 325, 74

Saunders, W., Rowan-Robinson, M., Lawrence, A., Efstathiou, G., Kaiser, N., Ellis, R. S., & Frenk, C. S. 1990, MNRAS, 242, 318

Saunders, W., et al. 2000, MNRAS, 317, 55
Schartmann, M., Meisenheimer, K., Camenzind, M., Wolf, S., & Henning, T. 2005, A&A, 437, 861
Scott, S. E., et al. 2002, MNRAS, 331, 817
Shakura, N. I., & Sunyaev, R. A. 1976, MNRAS, 175, 613
Silk, J. 2005, MNRAS, 364, 1337
Skinner, C. J., Smith, H. A., Sturm, E., Barlow, M. J., Cohen, R. J., & Stacey, G. J. 1997, Nature, 386, 472
Smail, I., Chapman, S. C., Blain, A. W., & Ivison, R. J. 2004, ApJ, 616, 71
Smail, I., Chapman, S. C., Ivison, R. J., Blain, A. W., Takata, T., Heckman, T. M., Dunlop, J. S., & Sekiguchi, K. 2003, MNRAS, 342, 1185
Smith, H. E., Lonsdale Carol, J., Lonsdale Colin, J., & Diamond, P. J. 1998, ApJ, 493, L17
Smith, J. D. T., & Houck, J. R. 2001, AJ, 121, 2115
Smith, J. D. T., et al. 2007, ApJ, 656, 770
Soifer, B. T., et al., 1984, ApJ, 283, L1
Spoon, H. W. W., Koornneef, J., Moorwood, A. F. M., Lutz, D., & Tielens, A. G. G. M. 2000, A&A, 357, 898
Spoon, H. W. W., et al. 2004, ApJS, 154, 184
———. 2006, ApJ, 638, 759
Stanford, S. A., Stern, D., van Breugel, W., & De Breuck, C. 2000, ApJS, 131, 185
Strauss, M. A., Davis, M., Yahil, A., & Huchra, J. P. 1990, ApJ, 361, 49
Sturm, E., Lutz, D., Verma, A., Netzer, H., Sternberg, A., Moorwood, A. F. M., Oliva, E., & Genzel, R. 2002, A&A, 393, 821
Sturm, E., et al. 1996, A&A, 315, L133
Swinbank, A. M., Chapman, S. C., Smail, I., Lindner, C., Borys, C., Blain, A. W., Ivison, R. J., & Lewis, G. F. 2006, MNRAS, 371, 465
Tacconi, L. J., Genzel, R., Lutz, D., Rigopoulou, D., Baker, A. J., Iserlohe, C., & Tecza, M. 2002, ApJ, 580, 73
Tacconi, L. J., et al. 2006, ApJ, 640, 228
Takata, T., Sekiguchi, K., Smail, I., Chapman, S. C., Geach, J. E., Swinbank, A. M., Blain, A., & Ivison, R. J. 2006, ApJ, 651, 713
Thornley, M. D., Schreiber, N. M. F., Lutz, D., Genzel, R., Spoon, H. W. W., Kunze, D., & Sternberg, A. 2000, ApJ, 539, 641
Thuan, T. X., Izotov, Y. I., & Foltz, C. B. 1999, ApJ, 525, 105
Tran, Q. D., et al. 2001, ApJ, 552, 527
Valiante, E., Lutz, D., Sturm, E., Genzel, R., Tacconi, L. J., Lehnert, M. D., & Baker, A. J. 2007, ApJ, 660, 1060
Veilleux, S., Kim, D.-C., & Sanders, D. B. 2002, ApJS, 143, 315
Veilleux, S., Kim, D.-C., Sanders, D. B., Mazzarella, J. M., & Soifer, B. T. 1995, ApJS, 98, 171
———. 1999, ApJ, 522, 139
Verma, A., Charmandaris, V., Klaas, U., Lutz, D., & Haas, M. 2005, Space Sci. Rev., 119, 355
Verma, A., Lutz, D., Sturm, E., Sternberg, A., Genzel, R., & Vacca, W. 2003, A&A, 403, 829
Voit, G. M. 1992, ApJ, 399, 495
Weedman, D. W., et al. 2005, ApJ, 633, 706
Werner, M. W., et al. 2004, ApJS, 154, 1
Wilman, R. J., Fabian, A. C., Cutri, R. M., Crawford, C. S., & Brandt, W. N. 1998, MNRAS, 300, L7
Wu, Y., Charmandaris, V., Hao, L., Brandl, B. R., Bernard-Salas, J., Spoon, H. W. W., & Houck, J. R. 2006, ApJ, 639, 157
Zauderer, B. A., Veilleux, S., & Yee, H. K. C. 2007, ApJ, 659, 1096